



Article

Joint Retrieval of Multiple Species of Ice Hydrometeor Parameters from Millimeter and Submillimeter Wave Brightness Temperature Based on Convolutional Neural Networks

Ke Chen ^{1,2,*} , Jiasheng Wu ¹ and Yingying Chen ¹

¹ School of Electronic Information and Communications, Huazhong University of Science and Technology, Wuhan 430074, China; u202014118@hust.edu.cn (Y.C.)

² Science and Technology on Multispectral Information Processing Laboratory, Wuhan 430074, China

* Correspondence: chenke@hust.edu.cn

Abstract: Submillimeter wave radiometers are promising remote sensing tools for sounding ice cloud parameters. The Ice Cloud Imager (ICI) aboard the second generation of the EUMETSAT Polar System (EPS–SG) is the first operational submillimeter wave radiometer used for ice cloud remote sensing. Ice clouds simultaneously contain three species of ice hydrometeors—ice, snow, and graupel—the physical distributions and submillimeter wave radiation characteristics of which differ. Therefore, jointly retrieving the mass parameters of the three ice hydrometeors from submillimeter brightness temperatures is very challenging. In this paper, we propose a multiple species of ice hydrometeor parameters retrieval algorithm based on convolutional neural networks (CNNs) that can jointly retrieve the total content and vertical profiles of ice, snow, and graupel particles from submillimeter brightness temperatures. The training dataset is generated by a numerical weather prediction (NWP) model and a submillimeter wave radiative transfer (RT) model. In this study, an end to end ICI simulation experiment involving forward modeling of the brightness temperature and retrieval of ice cloud parameters was conducted to verify the effectiveness of the proposed CNN retrieval algorithm. Compared with the classical Unet, the average relative errors of the improved RCNN–ResUnet are reduced by 11%, 25%, and 18% in GWP, IWP, and SWP retrieval, respectively. Compared with Bayesian Monte Carlo integration algorithm, the average relative error of the total content retrieved by RCNN–ResUnet is reduced by 71%. Compared with BP neural network algorithm, the average relative error of the vertical profiles retrieved by RCNN–ResUnet is reduced by 69%. In addition, this algorithm was applied to actual Advanced Technology Microwave Sounder (ATMS) 183 GHz observed brightness temperatures to retrieve graupel particle parameters with a relative error in the total content of less than 25% and a relative error in the profile of less than 35%. The results show that the proposed CNN algorithm can be applied to future space borne submillimeter wave radiometers to jointly retrieve mass parameters of ice, snow, and graupel.

Keywords: ice cloud remote sensing; submillimeter wave radiometer; convolutional neural networks; multiple species of ice hydrometeors; ice cloud imager (ICI)



Citation: Chen, K.; Wu, J.; Chen, Y. Joint Retrieval of Multiple Species of Ice Hydrometeor Parameters from Millimeter and Submillimeter Wave Brightness Temperature Based on Convolutional Neural Networks. *Remote Sens.* **2024**, *16*, 1096. <https://doi.org/10.3390/rs16061096>

Academic Editors: John Kalogiros, Jianzhong Lu and Marios Anagnostou

Received: 26 January 2024

Revised: 3 March 2024

Accepted: 17 March 2024

Published: 20 March 2024



Copyright: © 2024 by the authors. Licensee MDPI, Basel, Switzerland. This article is an open access article distributed under the terms and conditions of the Creative Commons Attribution (CC BY) license (<https://creativecommons.org/licenses/by/4.0/>).

1. Introduction

Ice clouds generally exist in the upper troposphere of the Earth's atmosphere at altitudes of 6 to 15 km [1] and are composed entirely or partially of ice particles [2]. Ice clouds play a critical role in the radiation budget and water cycle of the Earth, with the hydrological cycle being one of the most important subsystems in the atmosphere–ocean–climate system that supports life on Earth [3]. Accurate retrievals of ice cloud physical parameters (such as the ice water path (IWP) and ice water content (IWC) are crucial for understanding the radiative effects and climate impacts of ice clouds [4]. The ice hydrometeors in ice clouds contain three species: ice, snow, and graupel. Graupel is precipitation that occurs when supercooled water droplets in air collect and freeze on falling

snowflakes, forming 2–5 mm balls of crisp, opaque rime. Ice has many symmetrical shapes, including hexagonal columns, hexagonal plates, and dendritic crystals; it is responsible for various atmospheric optic displays and cloud formations. Snow comprises individual ice crystals that grow while suspended in the atmosphere—usually within clouds—and then fall, accumulating on the ground where they undergo further changes.

Compared to visible and infrared sensors, passive microwave sensors have superior all weather sounding capabilities [5] and are suitable for remote sensing ice clouds. Moreover, lower microwave frequencies lack sufficient sensitivity to small ice crystals within clouds [6]. The millimeter and submillimeter wavelengths ranging from 0.1 to 10 mm [7] are comparable to the sizes of ice hydrometeors in clouds (ice particles in ice clouds are mostly distributed from 20 to 600 μm [3]) and are sensitive to smaller ice hydrometeors, making them ideal frequencies for sounding ice clouds. Atmosphere sounding microwave radiometers include AMSU [8], MHS [9], and ATMS [10] onboard the National Oceanic and Atmospheric Administration (NOAA) and EUMETSAT MetOp satellites and MWHS [11] and MWTS [12] on the Chinese FengYun-3 satellite series. The highest frequency of these radiometers is limited to 183 GHz, restricting their ability to observe only ice clouds with large hydrometeors such as graupel. The ICI is the first sensor that uses millimeter and submillimeter waves for radiometric measurements of ice cloud parameters [13] and will be deployed on the EUMETSAT Polar System Second Generation (EPS-SG) [14] satellites by approximately 2026. Compared to the operational microwave sensors, ICI provides more frequency channels (from 183 GHz to 664 GHz) for sensing various ice hydrometeors.

The advantage of using a submillimeter wave radiometer for deriving ice cloud physical information was first noted by Evans and Graeme [15,16]. In the United States, an airborne ice cloud sensor, the compact scanning submillimeter wave imaging radiometer (CoSSIR), was developed, and a series of airborne experiments were conducted. Utilizing the Monte Carlo Bayesian algorithm, the IWC and IWP were retrieved from CoSSIR observations. This finding validates the ability of passive submillimeter wave technology to detect sounding ice clouds [17]. Jimenez et al. built an ice cloud database that included TBs (simulated brightness temperatures) ranging from 183 to 874 GHz using the Atmospheric Radiative Transfer Simulator (ARTS [18]) and retrieved IWPs using neural networks [19]. Weng and Grody indicated that under the premise of specifying the particle size distribution of ice hydrometeors, the D_{me} (the median mass equivalent size of a particle) and IWP parameters of ice clouds can be estimated from two-frequency millimeter/submillimeter brightness temperatures (e.g., 340 GHz and 89 GHz) [20]. Dong et al. proposed a Bayesian neural network (BNN)-based method to retrieve the IWP of ice clouds from submillimeter wave brightness temperatures [21]. Li et al. introduced a submillimeter retrieval algorithm based on the Voronoi ice crystal scattering model for retrieving ice cloud microphysical properties such as the IWP [22]. The current ice cloud parameter retrieval algorithms can achieve a relative error of approximately 50% for the IWP [23] and approximately 60% for the IWC [24].

Previous studies treated various ice hydrometeors as single ice particles. However, in the cloud microphysics model [25] and the RT model [18,26,27] of most operational NWP and data assimilation (DA) systems, ice hydrometeors include three species—ice, snow, and graupel—each with different submillimeter wave radiative transfer properties, making it difficult for traditional algorithms to jointly retrieve all three species of ice hydrometeors. CNNs [28] have strong feature extraction capabilities, and complex multilayer network structures provide powerful nonlinear fitting capabilities. CNNs have been extensively applied in remote sensing image classification and segmentation [29–31], and several studies have attempted to use CNNs for atmospheric parameter retrieval [32–35].

In this study, we innovatively employed CNNs to jointly retrieve physical parameters of ice, snow, and graupel particles in ice clouds from millimeter and submillimeter wave brightness temperatures, and the networks demonstrated strong generalization capabilities, producing accurate multiple species of ice hydrometeor retrievals under tropical cyclone conditions with different seasons and intensities. An end to end ICI simulation

experiment involving forward modeling of the brightness temperature and retrieval of ice cloud parameters was conducted to verify the effectiveness of the proposed CNN retrieval algorithm. Additionally, the CNN retrieval algorithm was applied to the actual ATMS 183 GHz brightness temperature to retrieve the graupel parameters.

The remainder of this article is organized as follows. Section 2 includes three subsections: simulated brightness temperature verification, ice cloud dataset construction, and TB generation. In Section 3, the proposed CNN algorithms, including the Unet and RCNN–ResUnet networks, are introduced. The experimental results and detailed analysis of both multiple species of ice cloud parameter retrieval from the simulated ICI data and graupel parameter retrieval from the actual ATMS observation data are presented and discussed in Section 4, while conclusions are drawn in Section 5.

2. Dataset

2.1. Simulated Brightness Temperature Verification

The reanalysis dataset ERA5 [36] developed by the European Centre for Medium–Range Weather Forecasts (ECMWF) was used as the atmospheric initialization field to run the Weather Research and Forecasting (WRF) model to conduct 6 h forecasts. Then, according to the frequency channels and observation geometry of ICI, the atmosphere and ice cloud parameters in the WRF output, including vertical profiles of pressure, temperature, relative humidity, and the hydrometeor content M (in g/m^3) for five hydrometeors (liquid, rain, ice, snow, and graupel), were input into the discrete ordinate tangent linear radiative transfer (DOTLRT) [27] model to simulate the ICI brightness temperature.

The WRF model uses 300×300 grids with $10 \text{ km} \times 10 \text{ km}$ resolution. The WRF latitude range of the SARIKA scenario (Figure 1) is $0\text{--}31^\circ\text{N}$, and the longitude range is $93\text{--}125^\circ\text{E}$. The parameterization schemes used are listed in Table 1.

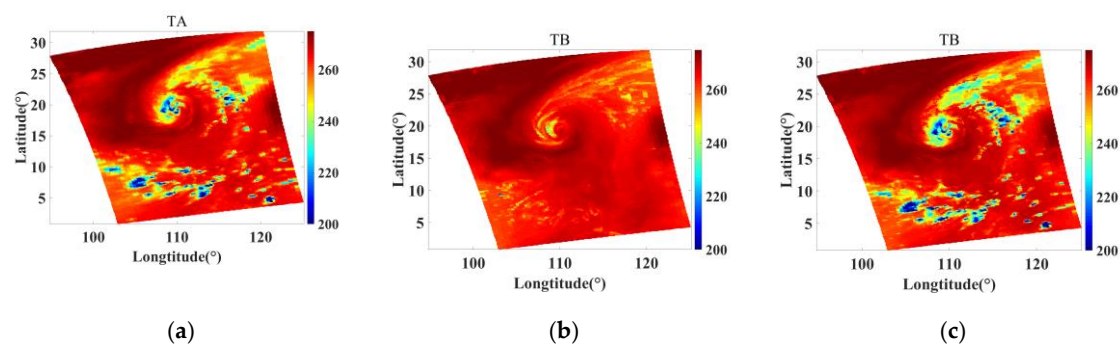


Figure 1. Brightness temperature (183.31 ± 7 GHz) comparison in the SARIKA scenario. (a) ATMS observed brightness temperature, (b) TB with WRF graupel data, and (c) TB with ATMS L2 graupel data.

Table 1. The parameterization schemes of WRF.

| Microphysics | Longwave Radiation | Shortwave Radiation | Surface Layer | Land Surface | Planetary Boundary Layer | Cumulus Parameterization |
|-------------------|--------------------|---------------------|----------------|-------------------------|--------------------------|--------------------------|
| Purdue Lin scheme | RRTM scheme | Dudhia scheme | MM5 similarity | Noah Land Surface Model | Yonsei University scheme | Kain–Fritsch scheme |

The DOTLRT model uses the discrete ordinate multiple stream method to solve the differential radiative transfer equation (DRTE) to calculate the upwelling apparent brightness temperature for a plane parallel atmosphere. DOTLRT uses the classical MPM93 model to calculate the absorption coefficient and the mie scattering method to calculate the scattering coefficient of five species of hydrometeors, including cloud liquid, rain, ice, snow, and graupel.

For validation, the simulation results were compared with the collocated actual ATMS observed brightness temperature. Only the highest 183 GHz band, which is sensitive to ice

clouds, was selected for comparison. Figure 1a shows the ATMS observed brightness temperature of Typhoon SARIKA at 183.31 ± 7 GHz, and Figure 1b shows the corresponding simulation. The simulated TB in the deep convection area of the typhoon is significantly different from the observed TB, the distribution of the surrounding spiral clouds is not consistent with the observed TB, and the cold temperature values of the ice clouds in the simulation are also significantly greater than those in the observation area, which indicates that the ice cloud parameters output by the WRF model are quite different from the actual values.

To improve the accuracy of the ice cloud dataset, the graupel mass profile PGraupel in the ATMS L2 product was introduced. PGraupel is the only valid ice cloud parameter in the ATMS L2 product [37], as 183 GHz is sensitive only to graupel particles [38]. Figures 2 and 3 show the horizontal and vertical mass distributions of graupel particles from the WRF output and ATMS L2 product for Typhoon SARIKA, where clear differences can be observed. Historically, numerical models tended to produce excessive amounts of large precipitation sized ice particles [39], and although some of these biases have been continuously reduced, they are still likely to exist and be positive. Figure 1c shows the simulated 183.31 ± 7 GHz brightness temperatures using NDE L2 graupel data instead of WRF graupel data. The simulated brightness temperature with ATMS L2 graupel data is obviously more consistent with the ATMS observation, and the scattering effect of the surrounding spiral ice cloud is also more obvious. Table 2 lists the root mean square errors (RMSEs) of the two TBs (using WRF and ATMS L2 graupel data) and the actual ATMS observations at channels 17–22 for eight tropical cyclone cases. The statistical analysis results are consistent with the visual effects. For all channels, the RMSEs of the simulation using ATMS L2 graupel data are markedly smaller than those using WRF graupel data, with reductions ranging from 29.39% to 78.16% for Typhoon SARIKA.

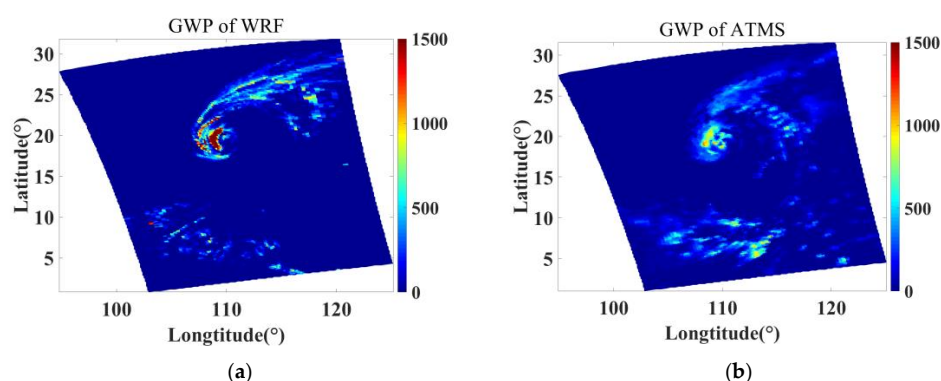


Figure 2. Comparison of the horizontal distribution of graupel in the SARIKA scenario. (a) Graupel data from the WRF model, and (b) graupel data from the ATMS L2 product.

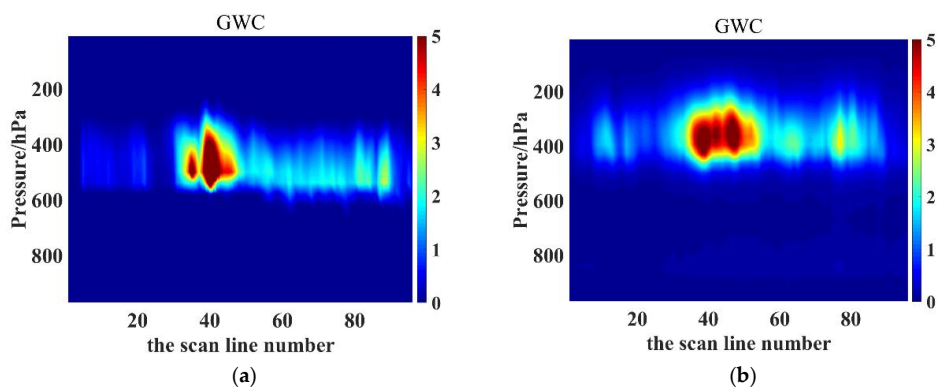


Figure 3. Comparison of the vertical distribution of graupel in the SARIKA scenario. (a) Graupel data from the WRF model, and (b) graupel data from the ATMS L2 product.

Table 2. Comparison of the RMSEs (K) of the simulated brightening temperature (WRF graupel data and ATMS L2 graupel data) and ATMS observation in the 165 GHz and 183 GHz band for eight tropical cyclone cases.

| | | Support | 165.5 | 183.31 ± 7 | 183.31 ± 4.5 | 183.31 ± 3 | 183.31 ± 1.8 | 183.31 ± 1 |
|-----------|--------------|---------|-------|------------|--------------|------------|--------------|------------|
| | | Surface | | | | | | |
| SARIKA | WRF data | | 14.58 | 10.51 | 7.68 | 5.61 | 4.00 | 3.13 |
| | ATMS L2 data | | 4.37 | 3.22 | 2.93 | 2.55 | 2.18 | 2.21 |
| NOCK-TEN | WRF data | | 11.03 | 8.57 | 6.69 | 5.21 | 3.82 | 2.92 |
| | ATMS L2 data | | 3.55 | 2.65 | 2.40 | 2.17 | 1.88 | 1.80 |
| NEOGURI | WRF data | | 13.28 | 11.10 | 9.13 | 7.40 | 5.71 | 4.40 |
| | ATMS L2 data | | 2.90 | 3.24 | 3.12 | 2.92 | 2.57 | 2.48 |
| FENGSHEN | WRF data | | 13.42 | 10.82 | 8.72 | 6.86 | 4.99 | 3.66 |
| | ATMS L2 data | | 3.35 | 3.43 | 3.18 | 2.83 | 2.35 | 2.18 |
| FUNG-WONG | WRF data | | 12.42 | 9.91 | 8.09 | 6.47 | 4.87 | 3.72 |
| | ATMS L2 data | | 4.42 | 3.26 | 2.79 | 2.38 | 2.00 | 2.02 |
| NANGKA | WRF data | | 9.75 | 8.16 | 6.76 | 5.56 | 4.45 | 3.64 |
| | ATMS L2 data | | 2.61 | 2.57 | 2.65 | 2.70 | 2.58 | 2.48 |
| CHAMPI | WRF data | | 8.58 | 7.33 | 6.15 | 5.07 | 3.95 | 3.18 |
| | ATMS L2 data | | 2.81 | 2.05 | 1.90 | 1.81 | 1.77 | 1.94 |
| MINDULLE | WRF data | | 17.81 | 13.51 | 10.38 | 7.83 | 5.66 | 4.20 |
| | ATMS L2 data | | 4.35 | 3.58 | 3.13 | 2.69 | 2.25 | 2.18 |

The TB verification experiments indicate the following: (1) compared with those in the WRF graupel data, the graupel mass profiles in the ATMS L2 products are more consistent with reality; (2) the presence of graupel particles in ice clouds has the most obvious influence on the brightness temperature in the 183 GHz band; and (3) the TBs simulated by the DOTLRT model can accurately calculate the scattering characteristics of ice clouds in the deep convection area of typhoons. Therefore, in this study, WRF output data were combined with ATMS L2 graupel data to construct a synthetic ice cloud database.

2.2. Construction of the Ice Cloud Dataset

The process for establishing the ice cloud dataset was as follows: first, historical tropical cyclone track data along China's eastern coast were downloaded from official meteorological websites (<https://tcddata.typhoon.org.cn/zjljsj.html>, accessed on 19 March 2024); next, the ATMS observations containing the tropical cyclones were obtained from NOAA's website (<https://www.avl.class.noaa.gov/saa/products/welcome>, accessed on 19 March 2024); then, the atmospheric and ice cloud parameters matching with the ATMS data in time and space were generated using the WRF model; finally, the graupel profiles in the WRF data were replaced by the PGraupel in ATMS L2 products to form a synthetic ice cloud dataset containing graupel, ice, and snow parameters.

The dataset covers all tropical cyclones passing through China's coastal regions from 2016 to 2022 with data augmentation by rotation, and the training set contains 2686 ice cloud scenarios after rotation (there were 1343 scenarios before rotation). As shown in Table 3, the China Meteorological Administration (CMA) categorizes tropical cyclones into six levels based on the maximum mean wind speeds near the surface center. According to the classification criteria, the proportion of tropical cyclones in each intensity category in the dataset is shown in Figure 4. The proportions of tropical cyclones in each intensity category were ranked from high to low as follows: Tropical Storm (TS, 29.08%), Tropical Depression (TD, 21.77%), Typhoon (TY, 15.48%), Severe Tropical Storm (STS, 14.70%), Strong Typhoon (STY, 11.31%), and Super Typhoon (Super TY, 7.65%). To validate the generalization

capability of the CNN networks, the test set includes tropical cyclone scenarios across all intensity levels, as listed in Table 4.

Table 3. Classification of tropical cyclone intensities by the CMA.

| Name | Stats |
|-----------------------------|---|
| Tropical Depression (TD) | Maximum mean wind speeds near the surface center of 10.8–17.1 m/s, corresponding to Level 6–7. |
| Tropical Storm (TS) | Maximum mean wind speeds near the surface center of 17.2–24.4 m/s, corresponding to Level 8–9. |
| Severe Tropical Storm (STS) | Maximum mean wind speeds near the surface center of 24.5–32.6 m/s, corresponding to Level 10–11. |
| Typhoon (TY) | Maximum mean wind speeds near the surface center of 32.7–41.4 m/s, corresponding to Level 12–13. |
| Strong typhoon (STY) | Maximum mean wind speeds near the surface center of 41.5–50.9 m/s, corresponding to Level 14–15. |
| Super typhoon (Super TY) | Maximum mean wind speeds near the surface center ≥ 51.0 m/s, corresponding to Level 16 or above. |

Table 4. List of tropical cyclones in the test set.

| Serial Number | Name | Time | Maximum Mean Wind Speed (m/s) | Grade Strength |
|---------------|-----------|------------------------|-------------------------------|----------------|
| 1 | SARIKA | 18 October 2016 05:50 | 33 | TY |
| 2 | NOCK-TEN | 24 December 2016 05:00 | 58 | Super TY |
| 3 | NEOGURI | 19 October 2019 15:00 | 42 | STY |
| 4 | FENGSHEN | 15 November 2019 15:50 | 50 | STY |
| 5 | FUNG-WONG | 20 November 2019 16:40 | 18 | TS |
| 6 | NANGKA | 12 October 2020 03:40 | 18 | TS |
| 7 | CHAMPI | 21 June 2021 15:50 | 13 | TD |
| 8 | MINDULLE | 5 October 2021 05:10 | 25 | STS |

The distributions of ice cloud parameters in different global climate models (GCMs) can vary by up to an order of magnitude, which is a major source of uncertainty in current atmospheric numerical models. These differences mainly originate from different assumptions about frozen particle characteristics and thresholds for the conversion of cloud ice to precipitation across models [40]. To improve climate and weather forecasting capabilities, ice cloud parameters must be observed at a global scale [3], including vertical profiles of ice water content (XWC) for different particle types and path integrated quantities (XWP, where X can represent different particle types such as G for graupel, I for ice, and S for snow). The specific definitions of these parameters are provided below.

The XWC refers to the vertical profile of the ice particle content, which represents the density distribution of ice particles with height in units of g/m^3 .

The XWP is the total path of the ice cloud and is the integral of the XWC in height, in g/m^2 , defined as follows:

$$XWP = \int XWC dz \quad (1)$$

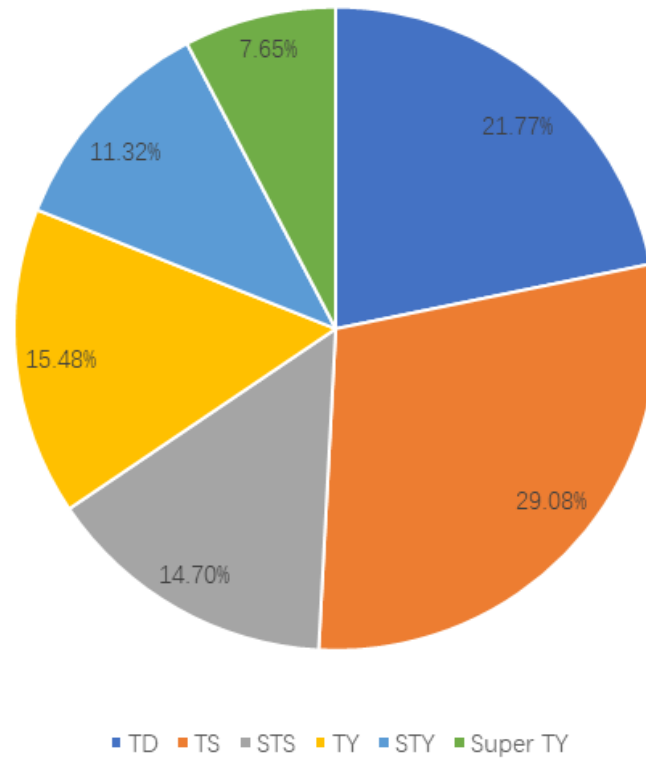


Figure 4. The proportion of tropical cyclones in each intensity category in the dataset.

2.3. Constructing the TB Dataset

To verify the performance of the proposed CNN retrieval algorithm, we carried out experiments on the joint retrieval of XWP and XWC from ice, snow, and graupel from simulated ICI TBs and the retrieval of graupel parameters from the actual ATMS 183 GHz observed TB. Therefore, we constructed two simulated brightness temperature datasets, namely, the ICI TB and ATMS 183 GHz TB (as shown in Tables 5 and 6, Figures 5 and 6), both of which were generated from the ice cloud dataset described in Section 2.2. The two simulated TB and ice cloud datasets constitute the training dataset, which is used to train CNNs to retrieve ice cloud parameters from ICI simulations and ATMS observations, respectively.

Table 5. ATMS graupel related frequency channels.

| Channel Number | Center Frequency (GHz) | Equivalent Noise Temperature Difference (K) |
|----------------|------------------------|---|
| 17 | 165.5 | 0.6 |
| 18 | 183.31 ± 7 | 0.8 |
| 19 | 183.31 ± 4.5 | 0.8 |
| 20 | 183.31 ± 3 | 0.8 |
| 21 | 183.31 ± 1.8 | 0.8 |
| 22 | 183.31 ± 1 | 0.9 |

Table 6. ICI frequency channels.

| Channel Number | Center Frequency (GHz) | Equivalent Noise Temperature Difference (K) |
|----------------|------------------------|---|
| 1 | 183.31 ± 7.0 | 0.8 |
| 2 | 183.31 ± 3.4 | 0.8 |
| 3 | 183.31 ± 2.0 | 0.8 |
| 4 | 243.2 ± 2.5 | 0.7 |
| 5 | 325.15 ± 9.5 | 1.2 |
| 6 | 325.15 ± 3.5 | 1.3 |
| 7 | 325.15 ± 1.5 | 1.5 |
| 8 | 448 ± 7.2 | 1.4 |

Table 6. Cont.

| Channel Number | Center Frequency (GHz) | Equivalent Noise Temperature Difference (K) |
|----------------|------------------------|---|
| 9 | 448 ± 3.0 | 1.6 |
| 10 | 448 ± 1.4 | 2.0 |
| 11 | 664 ± 4.2 | 1.6 |

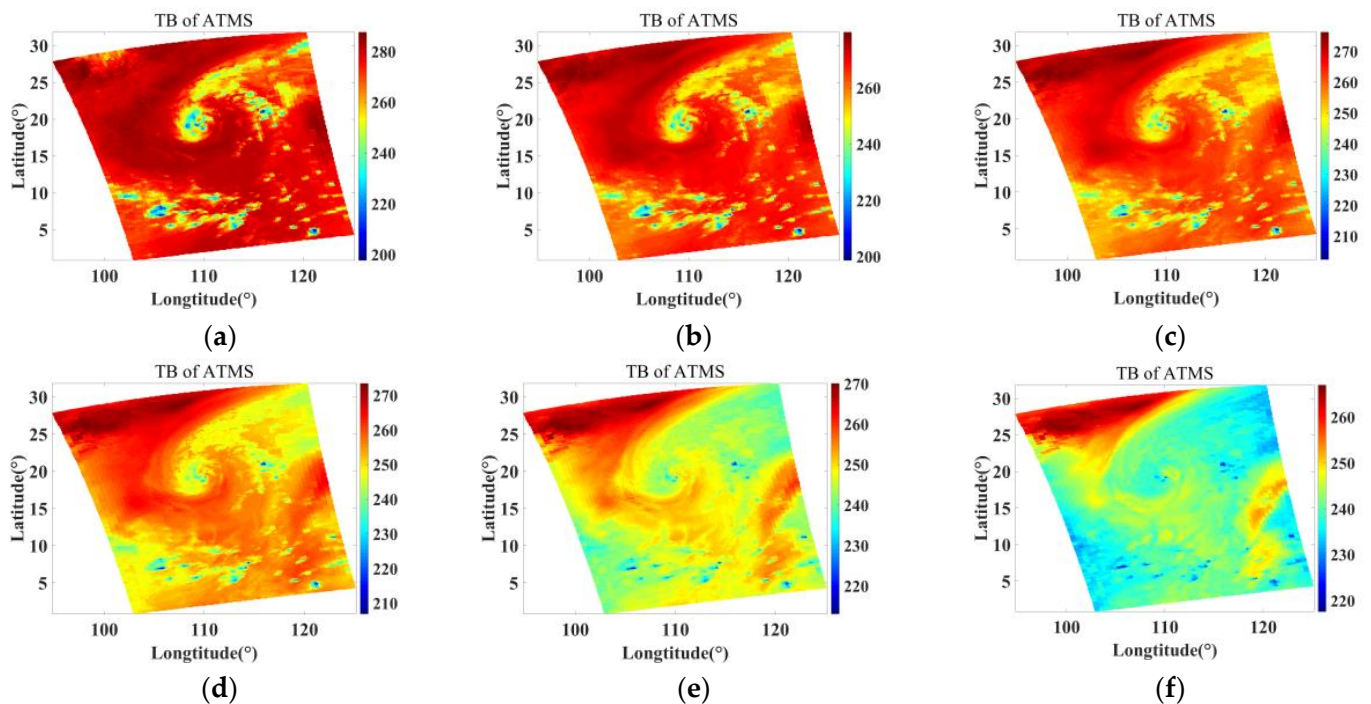


Figure 5. Simulated ATMS TBs of Typhoon SARIKA in the dataset: (a) 165.5 GHz; (b) 183.31 ± 7 GHz; (c) 183.31 ± 4.5 GHz; (d) 183.31 ± 3 GHz; (e) 183.31 ± 1.8 GHz; and (f) 183.31 ± 1.8 GHz.

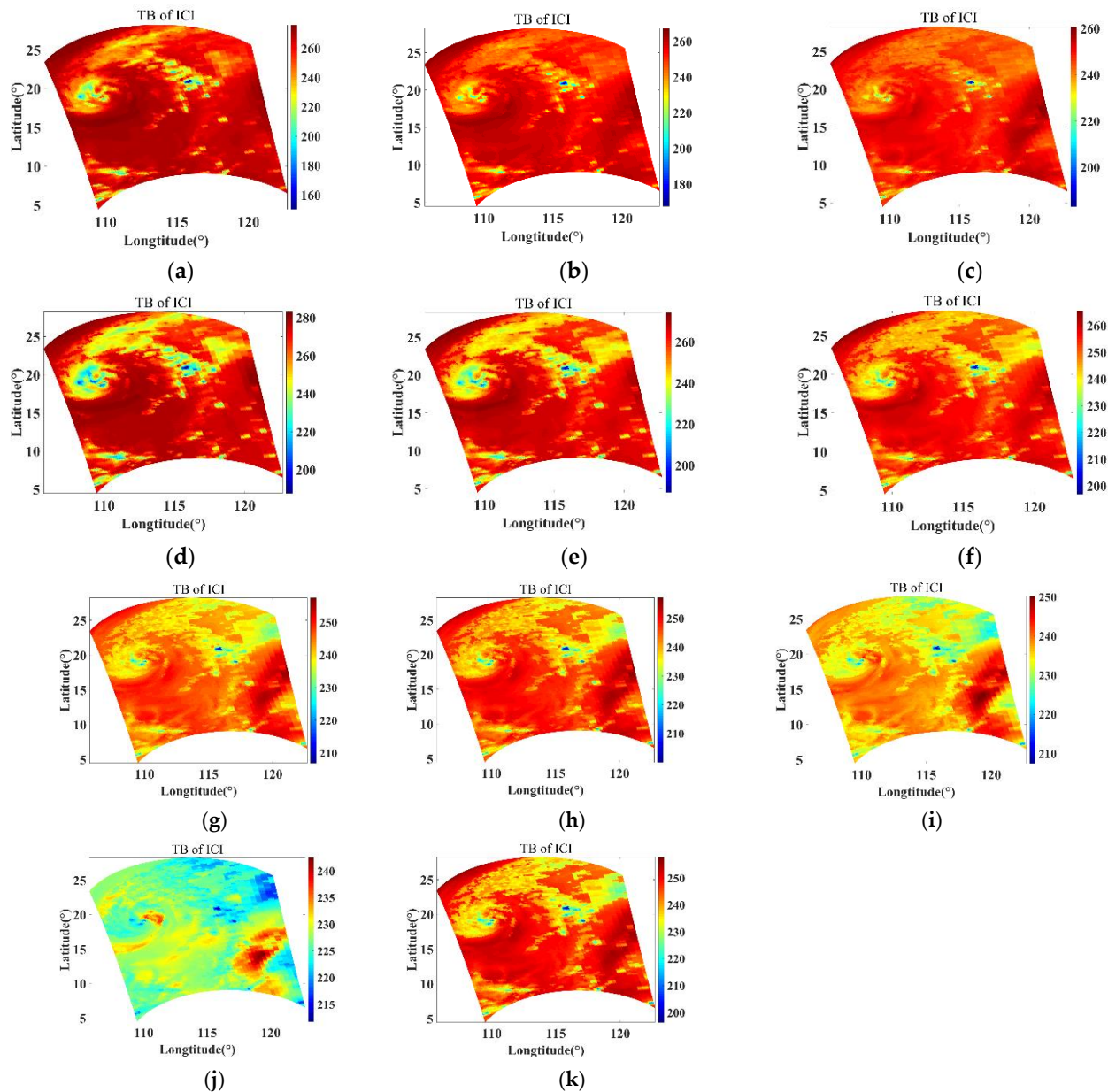


Figure 6. Simulated ICI TBs of Typhoon SARIKA in the dataset: (a) 183.31 ± 7.0 GHz; (b) 183.31 ± 3.4 GHz; (c) 183.31 ± 2.0 GHz; (d) 243.2 ± 2.5 GHz; (e) 325.15 ± 9.5 GHz; (f) 325.15 ± 3.5 GHz; (g) 325.15 ± 1.5 GHz; (h) 448 ± 7.2 GHz; (i) 448 ± 3.0 GHz; (j) 448 ± 1.4 GHz; and (k) 664 ± 4.2 GHz.

3. Algorithm Introduction

3.1. Unet

The Unet network [41] is a convolutional neural network with an encoder–decoder structure that was proposed by Olaf Ronneberger et al. in 2015; its name comes from the U shape of the network architecture. Unet was originally used for medical image segmentation. After its proposal, many studies built new models on the basis of Unet for new applications [42–45]. In this work, the Unet network was utilized for ice cloud parameter retrieval as a benchmark algorithm.

As shown in Figure 7, the characteristics of the Unet network include the following: 1. The network structure consists of an encoder–decoder architecture, the encoder comprises multiple downsampling layers to extract features and contextual information from the input image, and the decoder consists of upsampling layers to gradually recover the resolution

of the feature maps; 2. The encoder and decoder are connected through skip connections to enable feature reuse, retaining spatial information from the original image—this approach is beneficial for segmentation and localization prediction; 3. Before each downsampling, the number of channels in the feature map is doubled to capture additional semantic information, upsampling reduces the number of channels; 4. The network contains no fully connected layers and contains only convolutional, pooling, and other operations, making it more suitable for processing spatial information; 5. End to end training eliminates the need for complex pre/postprocessing.

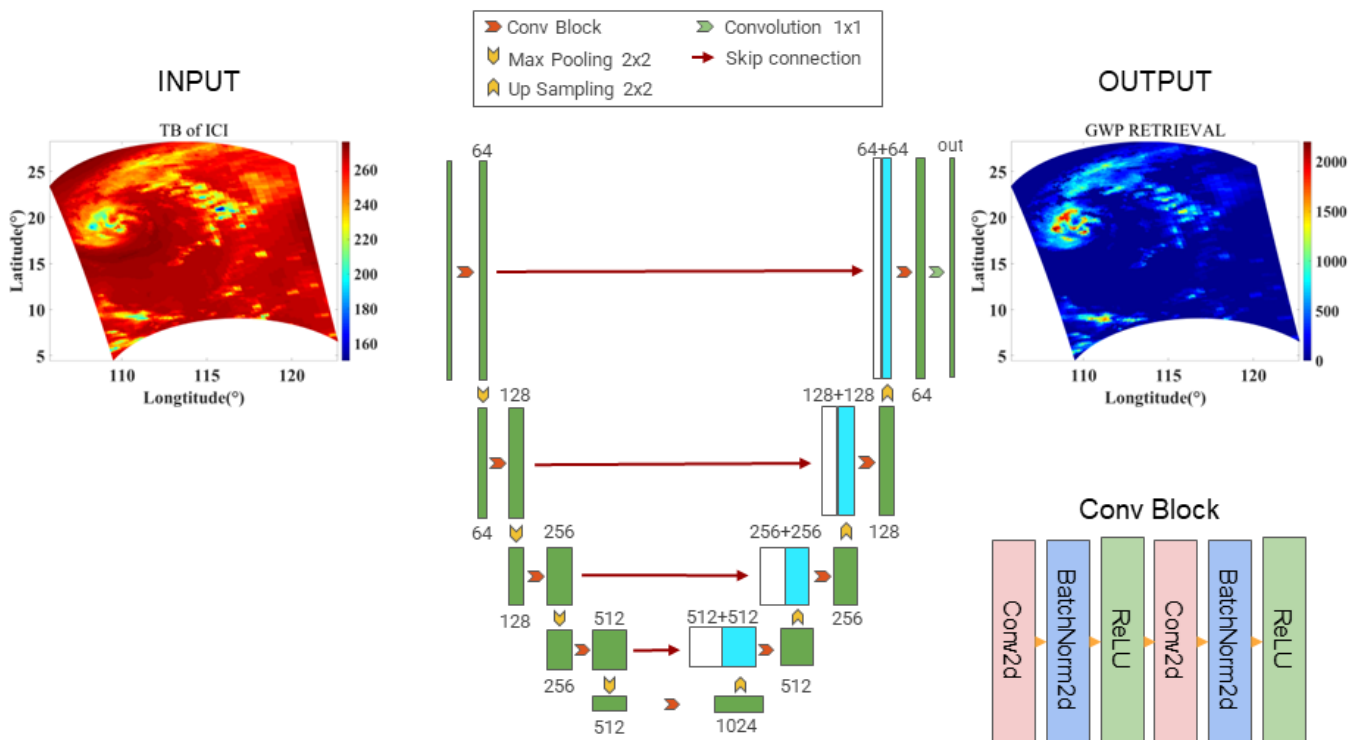


Figure 7. Unet network structure.

3.2. RCNN–ResUnet

On the basis of the original Unet network, we incorporated recurrent convolutional layers [46] and residual structure design [47] to construct the RCNN–ResUnet network architecture, as shown in Figures 8 and 9. Specifically, the encoder and decoder modules in RCNN–ResUnet both employ recurrent convolutional layers instead of regular convolution layers. Recurrent convolutional layers can accumulate feature information, which is beneficial for image-related tasks. In addition, RCNN–ResUnet inserts residual units after the recurrent convolutional layers to form recurrent residual convolutional modules. The residual structure facilitates the training of deeper models.

Compared to the original Unet, the advantages of RCNN–ResUnet include the following: 1. Recurrent convolutional layers can accumulate features, enhancing feature representation; 2. The residual structure mitigates gradient vanishing, facilitating training of deeper networks; 3. Without increasing the number of parameters, the retrieval accuracy improved.

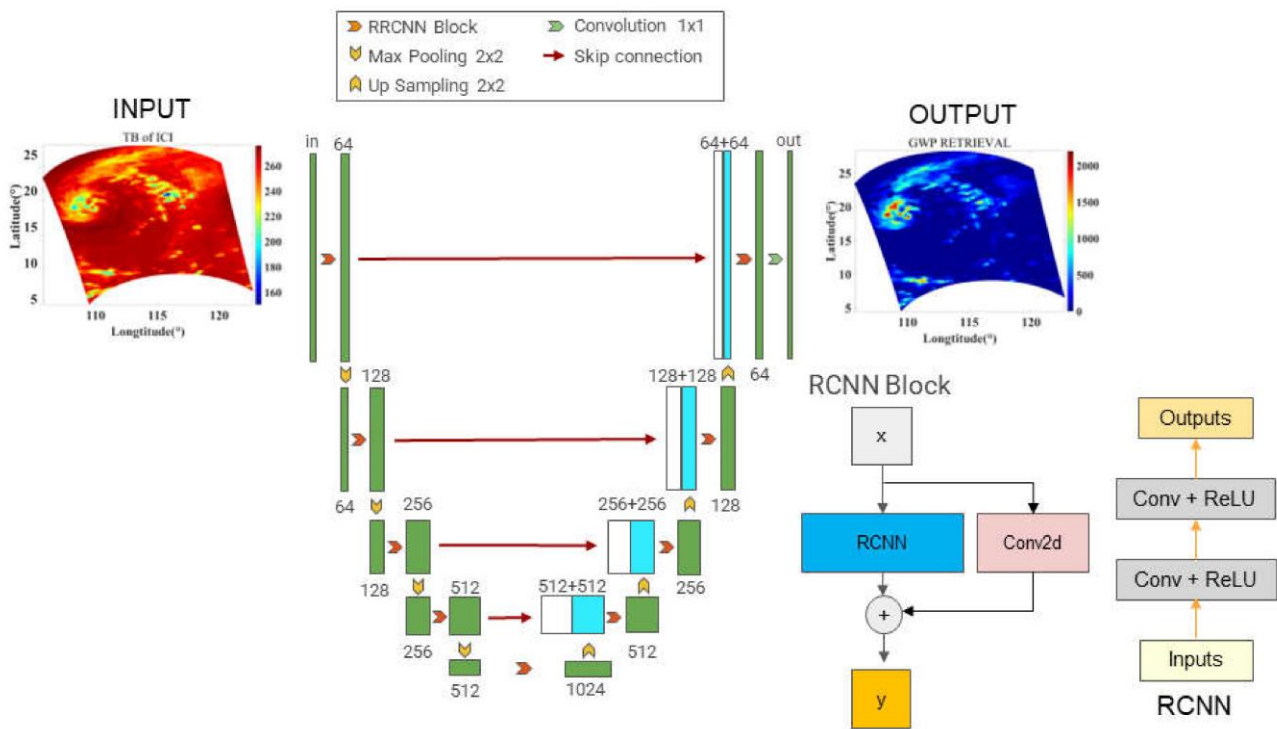


Figure 8. The structural design of RCNN-ResUnet, including RCNN Block and RCNN.

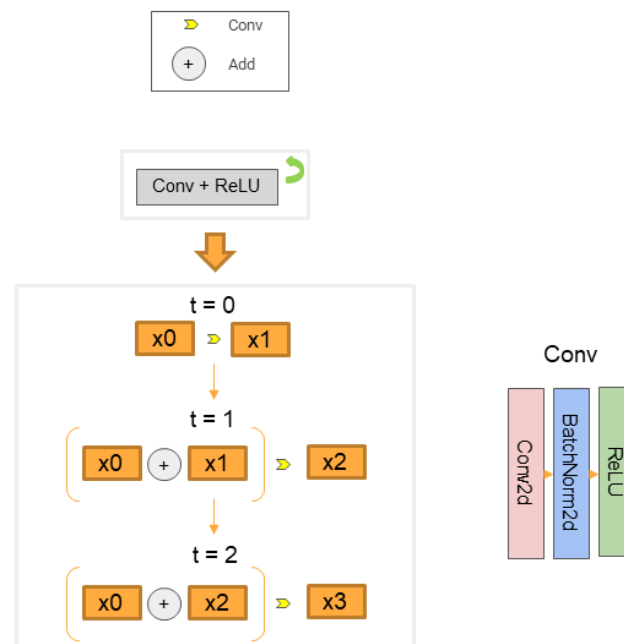


Figure 9. Structural design of the cyclic convolution layer.

4. Ice Cloud Parameter Retrieval Experiments

To verify the effectiveness and performance of the proposed CNN retrieval algorithms, two ice cloud retrieval experiments were conducted. First, the CNN retrieval algorithms applied the simulated ICI TB to jointly retrieve the physical parameters of ice, snow, and graupel. The retrieval objects are path integrated quantities (XWP) and vertical profiles of water content (XWC), where X represents different ice hydrometeors, such as I for ice, S for snow, and G for graupel. In addition, to verify the effectiveness of this algorithm on real satellite data, CNN algorithms were also applied to actual ATMS 183 GHz observed brightness temperatures to retrieve graupel parameters. Because the highest ATMS frequency

reaches only 183 GHz, previous studies have shown that this frequency is sensitive only to graupel particles and cannot measure ice and snow [24].

4.1. Multiple Species of Ice Hydrometeors Retrieval from the Simulated ICI Brightness Temperature

Figure 10 shows the experimental procedure for the joint retrieval of multiple species of ice hydrometeor parameters from the ICI simulation; the details are as follows:

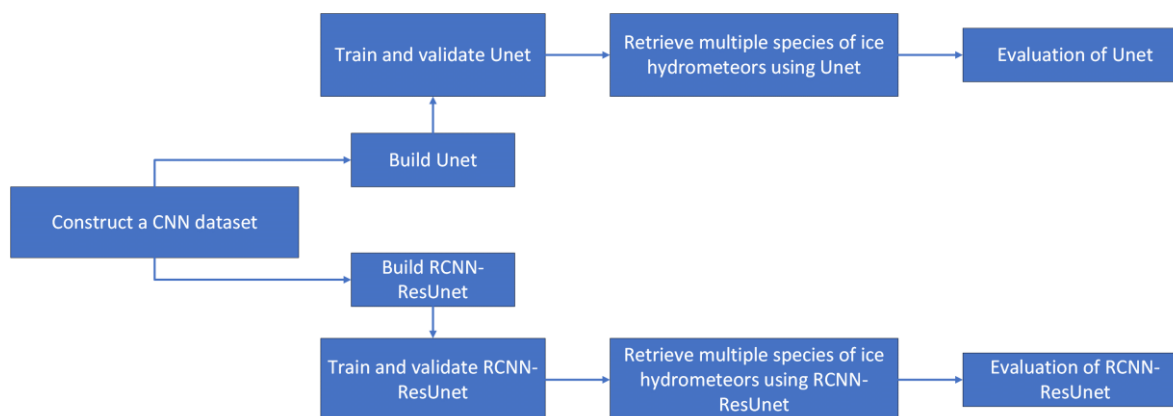


Figure 10. Flow chart of the joint retrieval of multiple species of ice hydrometeor parameters from ICI simulation.

Step 1: Construct the CNN dataset consisting of pairs of the synthetic ice cloud database and the corresponding simulated ICI brightness temperatures, as shown in Figure 6;

Step 2: Build the Unet and RCNN–ResUnet networks;

Step 3: The networks are trained and validated using the training set and validation set, respectively;

Step 4: The well trained Unet and RCNN–ResUnet networks are used to retrieve multiple species of ice hydrometeor parameters from the ICI simulation in the test set. The test set includes eight tropical cyclone scenarios across all intensity levels, as listed in Table 4.

Step 5: The multiple species of ice hydrometeor parameters in the test set are used as the “reference truth” to evaluate the retrieval errors.

4.1.1. Joint Retrieval of Water Paths of Multiple Species of Ice Hydrometeors

First, the CNN algorithm was applied to simulate the ICI brightness temperatures to jointly retrieve the path integrated quantities of the three ice hydrometeors: GWP, IWP, and SWP.

Figures 11–13 show the experimental results of jointly retrieving GWP, IWP, and SWP for the SARIKA scenario using Unet and RCNN–ResUnet, respectively, where (a) is the “reference truth” in the test data, (b) is the retrieval result of Unet, (c) is the retrieval result of RCNN–ResUnet, (d) is the scatter plot of RCNN–ResUnet retrieval, (e) is the error of Unet retrieval and (f) is the error of RCNN–ResUnet retrieval. It can be seen that for ice, snow, and graupel particles, both Unet and RCNN–ResUnet can accurately retrieve the spatial distribution characteristics of GWP, IWP, and SWP.

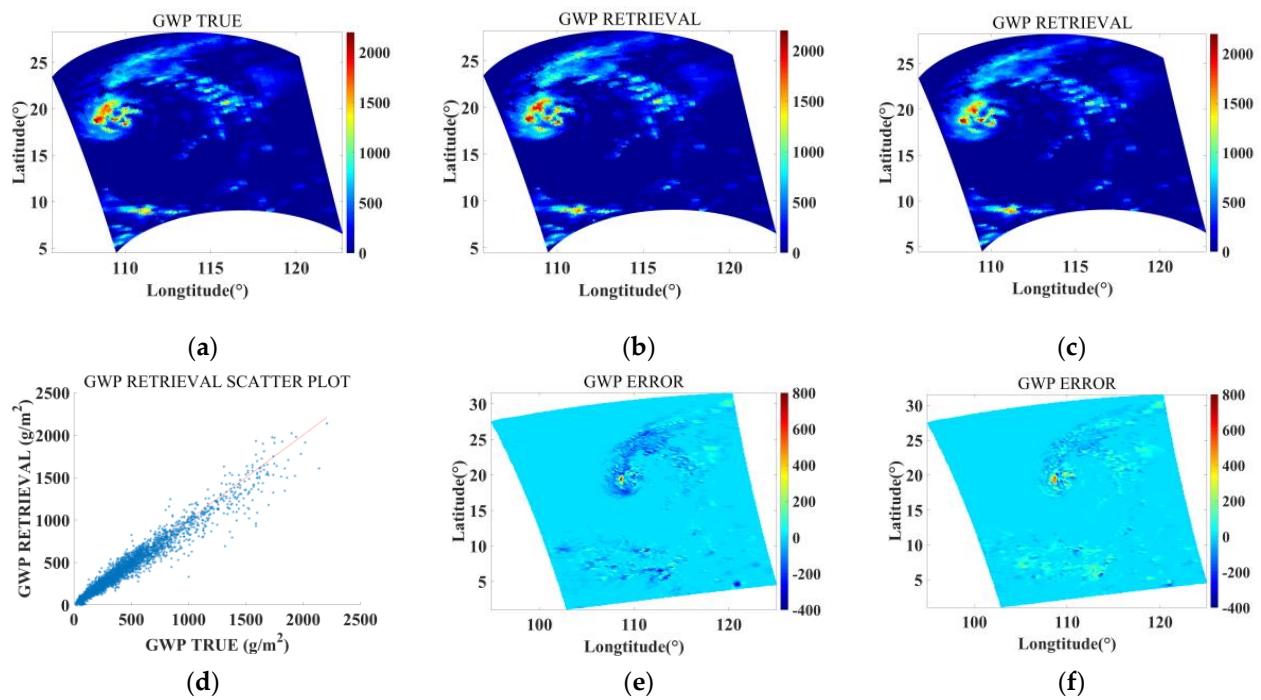


Figure 11. GWP retrieval results for Typhoon SARIKA. (a) The reference truth; (b) Unet retrieval; (c) RCNN-ResUnet retrieval; (d) scatter plot of RCNN-ResUnet retrieval; (e) error of Unet retrieval; and (f) error of RCNN-ResUnet retrieval. The red line in (d) represents the function $y = x$.

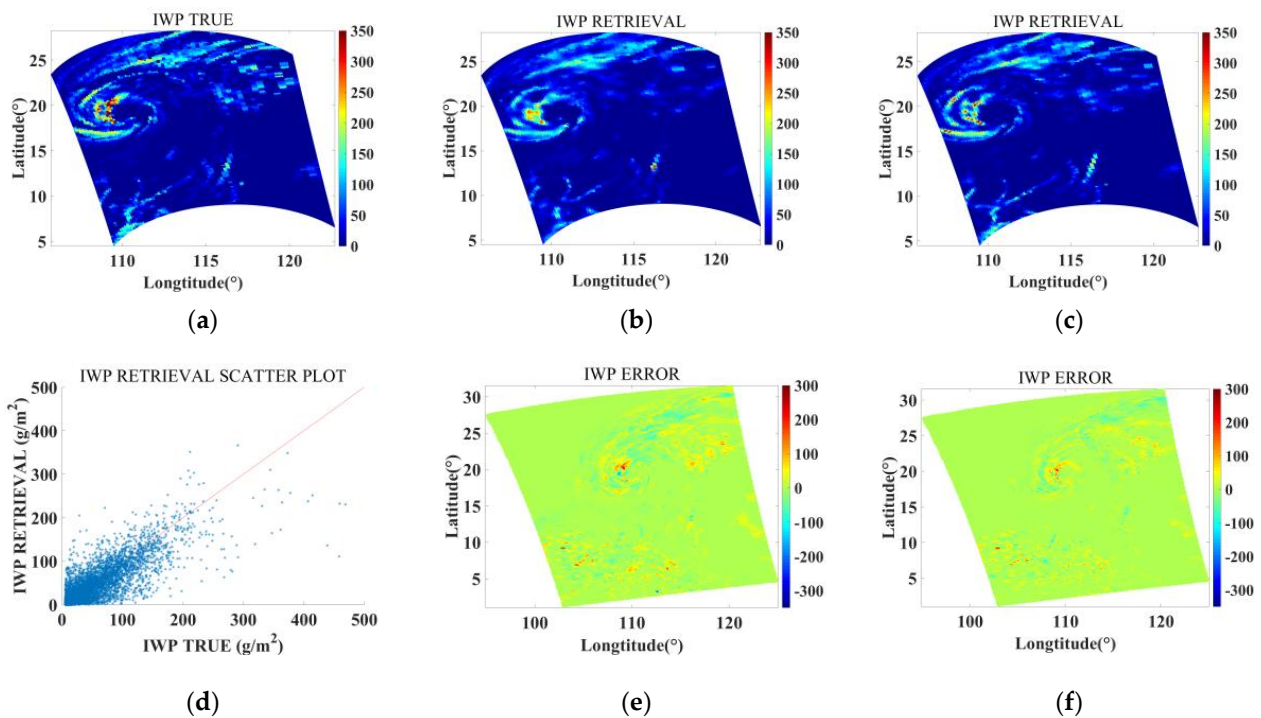


Figure 12. IWP retrieval results for Typhoon SARIKA. (a) The reference truth; (b) Unet retrieval; (c) RCNN-ResUnet retrieval; (d) scatter plot of RCNN-ResUnet retrieval; (e) error of Unet retrieval; and (f) error of RCNN-ResUnet retrieval. The red line in (d) represents the function $y = x$.

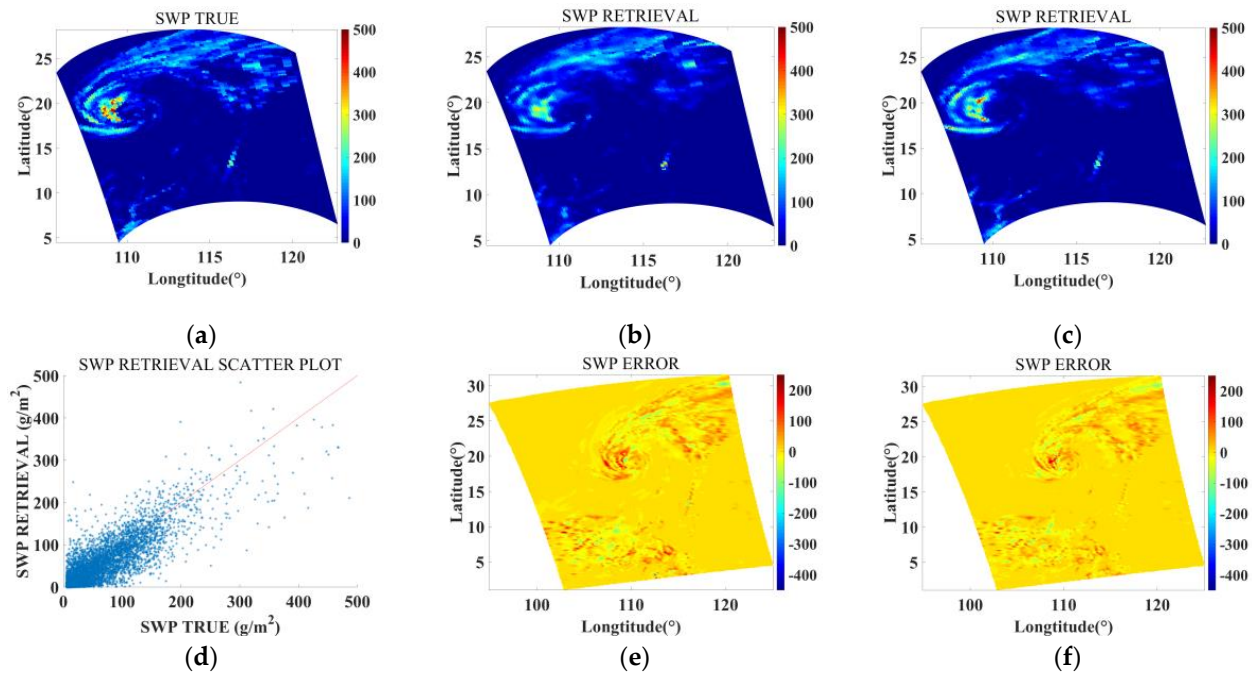


Figure 13. SWP retrieval results for Typhoon SARIKA. (a) The reference truth; (b) Unet retrieval; (c) RCNN–ResUnet retrieval; (d) scatter plot of RCNN–ResUnet retrieval; (e) error of Unet retrieval; and (f) error of RCNN–ResUnet retrieval. The red line in (d) represents the function $y = x$.

Figure 14a,b show the percentage errors of GWP, IWP, and SWP retrieved by Unet and RCNN–ResUnet, respectively, for all eight test scenarios. Using Unet, the relative error of the GWP is between 15% and 18% for all test data, with an average of 16.34%; the IWP relative error ranges from 62% to 79%, with an average of 68.2%; and the SWP relative error is between 54% and 83%, with an average of 69.14%. Using the RCNN–ResUnet, the relative error of the GWP is between 12% and 16%, with an average of 14.48%; the IWP relative error ranges from 47% to 58%, with an average of 51.38%; and the SWP relative error is between 45% and 65%, with an average of 57.01%.

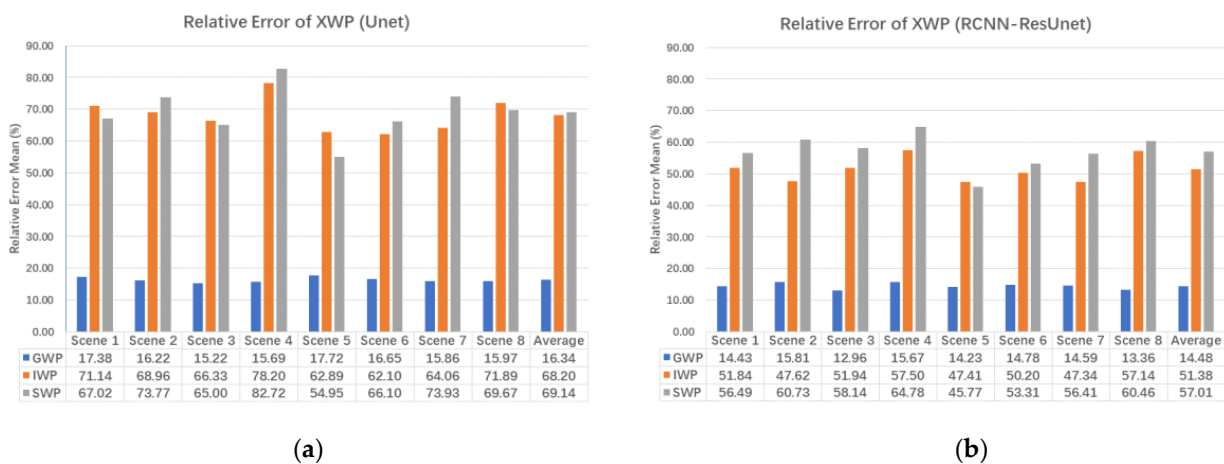


Figure 14. Relative errors in the GWP, IWP, and SWP for all eight tropical cyclone scenarios. (a) Unet and (b) RCNN–ResUnet.

Figure 14 indicates that the proposed CNN algorithms can effectively and jointly retrieve the path integrated quantities of graupel, ice, and snow particles from the ICI submillimeter wave brightness temperature. Compared with those of classical Unet, the

retrieval errors of the revised RCNN–ResUnet are significantly lower—11% for GWP, 25% for IWP, and 18% for SWP.

4.1.2. Joint Retrieval of Multiple Species of Ice Water Contents

Then, the CNN algorithms were applied to simulate the ICI brightness temperature to jointly retrieve the profiles of the water content of the three ice hydrometeors: GWC, IWC, and SWC.

Figures 15–17 show the retrieval results of GWC, IWC, and SWC for Typhoon SARIKA using Unet and RCNN–ResUnet, respectively, where (a) is the reference truth value, (b) is the retrieval result of Unet, (c) is the retrieval result of RCNN–ResUnet, (d) is the scatter plot of Unet retrieval, and (e) is the scatter plot of RCNN–ResUnet retrieval. For ice, snow, and graupel particles, both Unet and RCNN–ResUnet can retrieve the vertical distribution characteristics of the GWC, IWC, and SWC with good accuracy.

Figure 18a,b show the percentage errors of the GWC, IWC, and SWC retrieved by Unet and RCNN–ResUnet, respectively, for all eight test scenarios. Using Unet, the relative error in the GWC is between 28% and 38% for all test data, with an average of 32.78%; the IWC relative error ranges from 60% to 86%, with an average of 70.36%; and the SWC relative error is between 67% and 100%, with an average of 76.14%. Using the RCNN–ResUnet, the relative error of the GWC is between 14% and 22%, with an average of 18.41%; the IWC relative error ranges from 55% to 82%, with an average of 68.84%; and the SWC relative error is between 66% and 88%, with an average of 78.06%.

Figure 18 indicates that the proposed CNN algorithm can effectively and jointly retrieve the water content profiles of graupel, ice, and snow particles from the ICI submillimeter wave brightness temperature. Compared with that of Unet, the retrieval error of the revised RCNN–ResUnet is 44% lower for GWC and is almost the same for IWC and SWC.

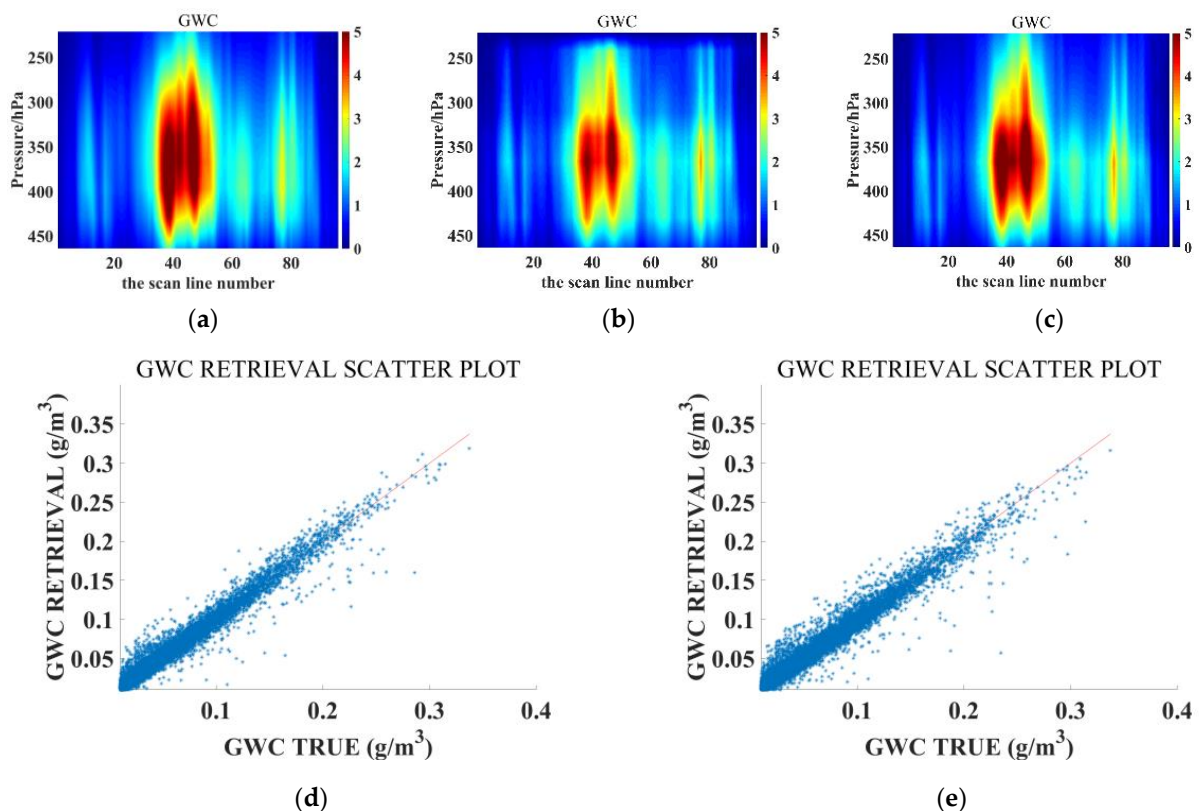


Figure 15. GWC retrieval results for Typhoon SARIKA. (a) The reference truth; (b) Unet retrieval; (c) RCNN–ResUnet retrieval; (d) scatter plot of Unet retrieval; and (e) scatter plot of RCNN–ResUnet retrieval. The red line in (d,e) represents the function $y = x$.

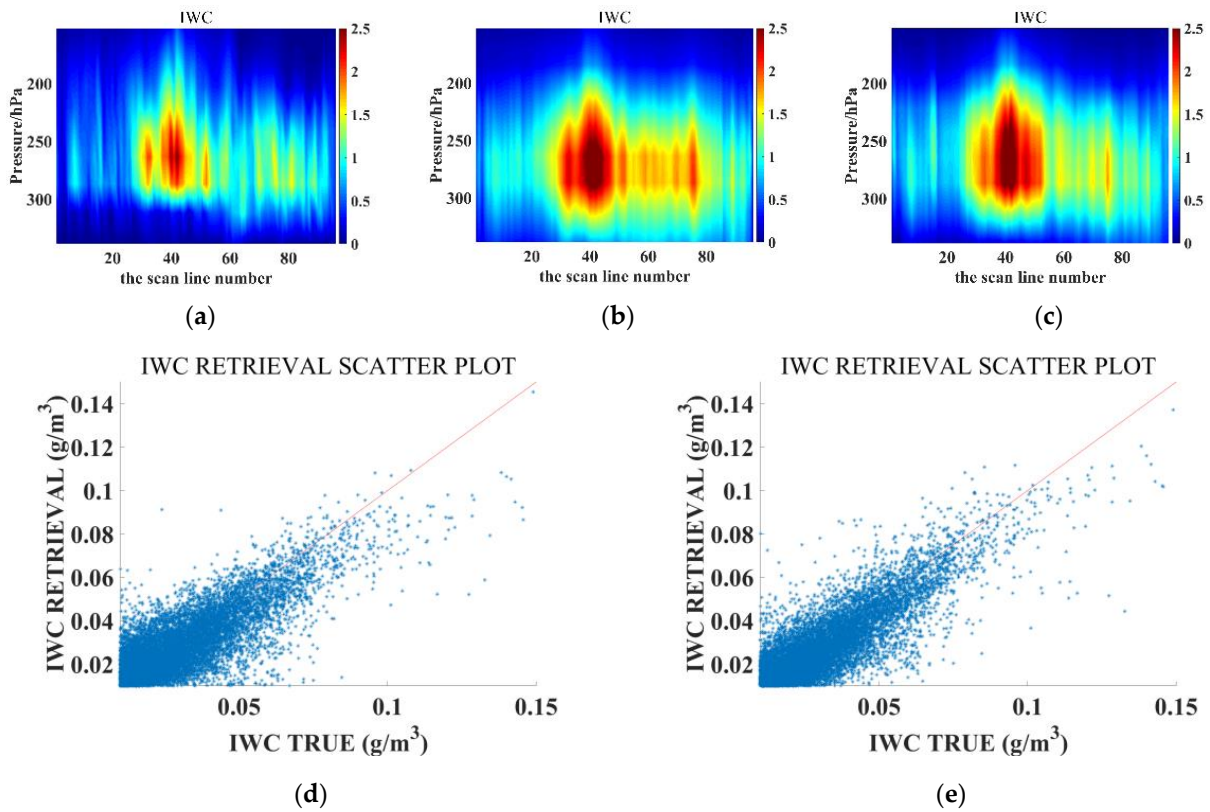


Figure 16. IWC retrieval results for Typhoon SARIKA. (a) The reference truth; (b) Unet retrieval; (c) RCNN-ResUnet retrieval; (d) scatter plot of Unet retrieval; (e) scatter plot of RCNN-ResUnet retrieval. The red line in (d,e) represents the function $y = x$.

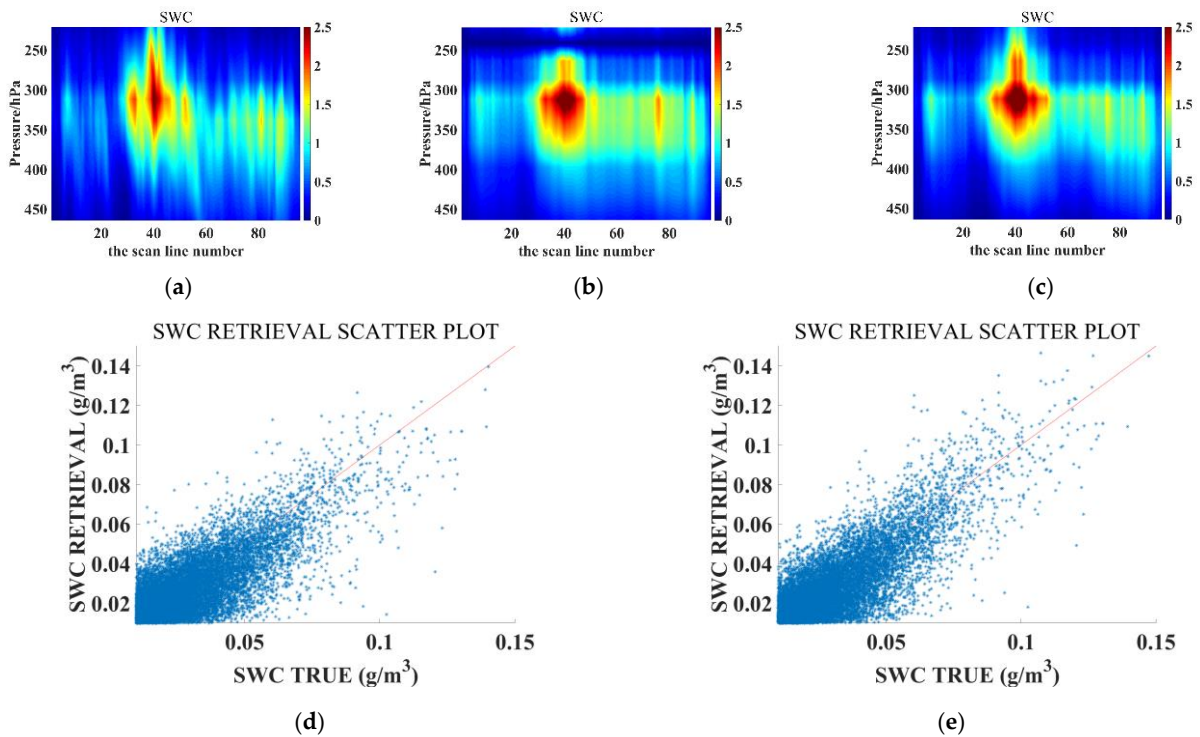


Figure 17. SWC retrieval results for Typhoon SARIKA. (a) The reference truth; (b) Unet retrieval; (c) RCNN-ResUnet retrieval; (d) scatter plot of Unet retrieval; and (e) scatter plot of RCNN-ResUnet retrieval. The red line in (d,e) represents the function $y = x$.

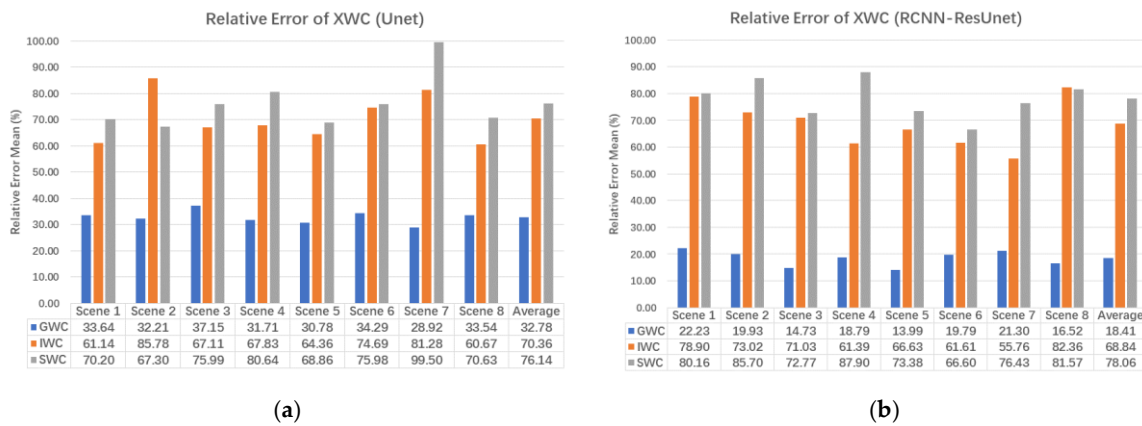


Figure 18. Relative errors in GWC, IWC, and SWC under the SARIKA scenario. (a) Unet and (b) RCNN-ResUnet.

4.2. Graupel Parameter Retrieval from the Actual ATMS Brightness Temperature

Figure 19 shows the experimental procedure for retrieving graupel parameters from the actual ATMS 183 GHz brightness temperature; the details are as follows:

Step 1: The CNN dataset consisting of pairs of synthetic ice cloud databases and corresponding simulated ATMS 183 GHz brightness temperatures is constructed, as shown in Figure 5;

Step 2: The Unet and RCNN-ResUnet networks are built;

Step 3: The networks are trained and validated using the training set and validation set, respectively;

Step 4: The well trained Unet and RCNN-ResUnet networks are applied to the ATMS simulation in the test set and corresponding ATMS observation to retrieve graupel parameters;

Step 5: The graupel parameters in the test set are used as the “reference truth” to evaluate the retrieval errors.

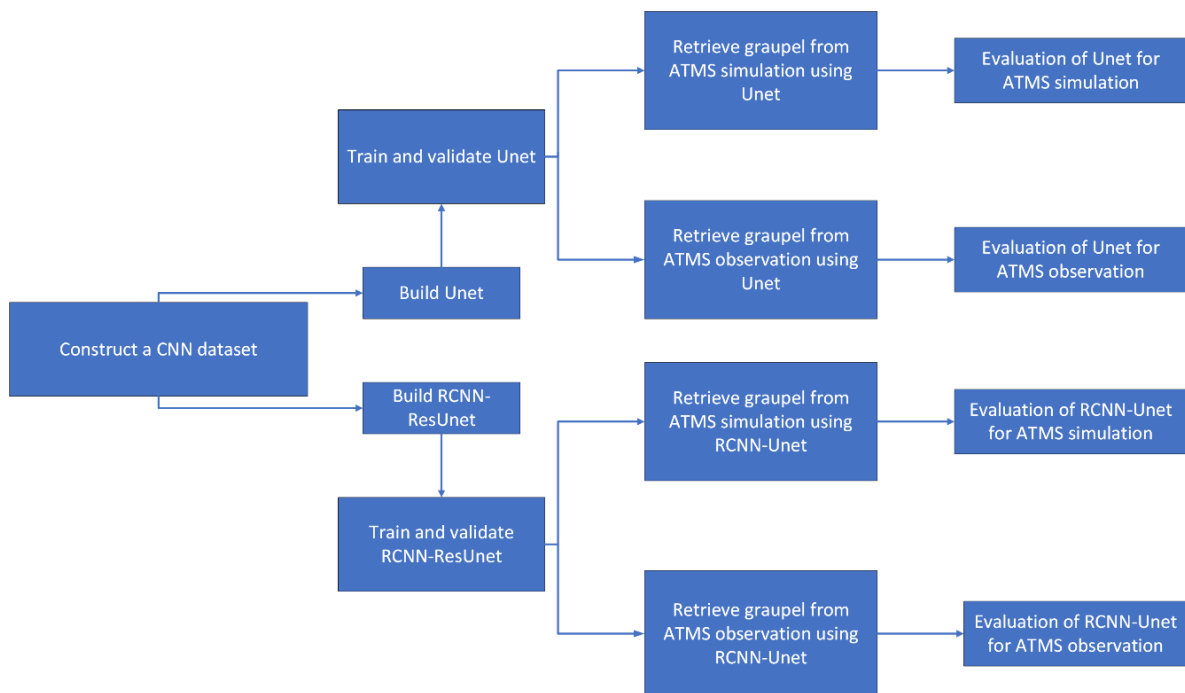


Figure 19. Flow chart of the retrieval of graupel parameters from ATMS observations.

4.2.1. Retrieval of the Graupel Water Path (GWP)

First, the CNN algorithms were applied to the simulated ATMS 183 GHz brightness temperature and the actual ATMS observation to retrieve the GWP.

Figure 20 shows the GWP retrieval experimental results of the ATMS simulation for Typhoon SARIKA using Unet and RCNN-ResUnet, where (a) is the “reference truth” in the test data, (b) is the retrieval result of Unet, and (c) is the retrieval result of RCNN-ResUnet. Figure 21 shows the GWP retrieval experimental results for the actual ATMS observations, where (a) is the “reference truth” in the test data, (b) is the retrieval result of Unet, (c) is the retrieval result of RCNN-ResUnet, (d) is the scatter plot of Unet retrieval and (e) is the scatter plot of RCNN-ResUnet retrieval. Even for the actual ATMS observations, both Unet and RCNN-ResUnet trained by the ATMS simulation can accurately retrieve the spatial distribution characteristics of the GWP.

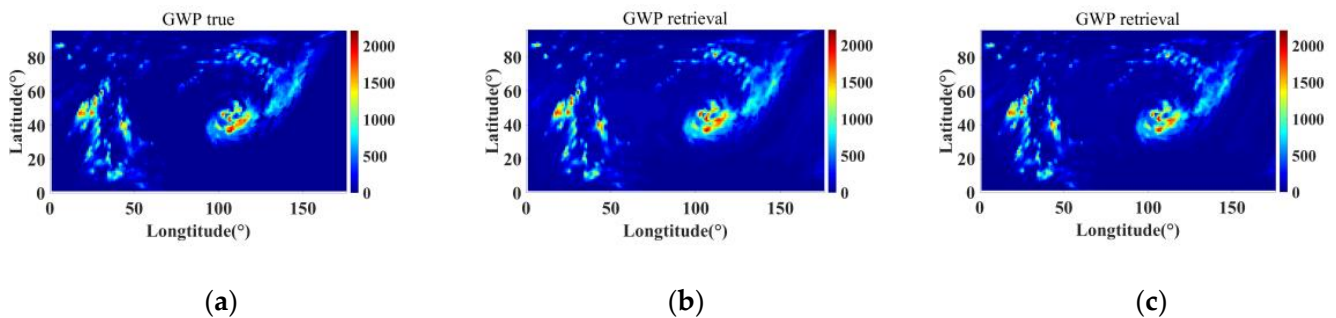


Figure 20. GWP retrieval results of the ATMS simulation. (a) Reference truth; (b) Unet retrieval; and (c) RCNN-ResUnet retrieval.

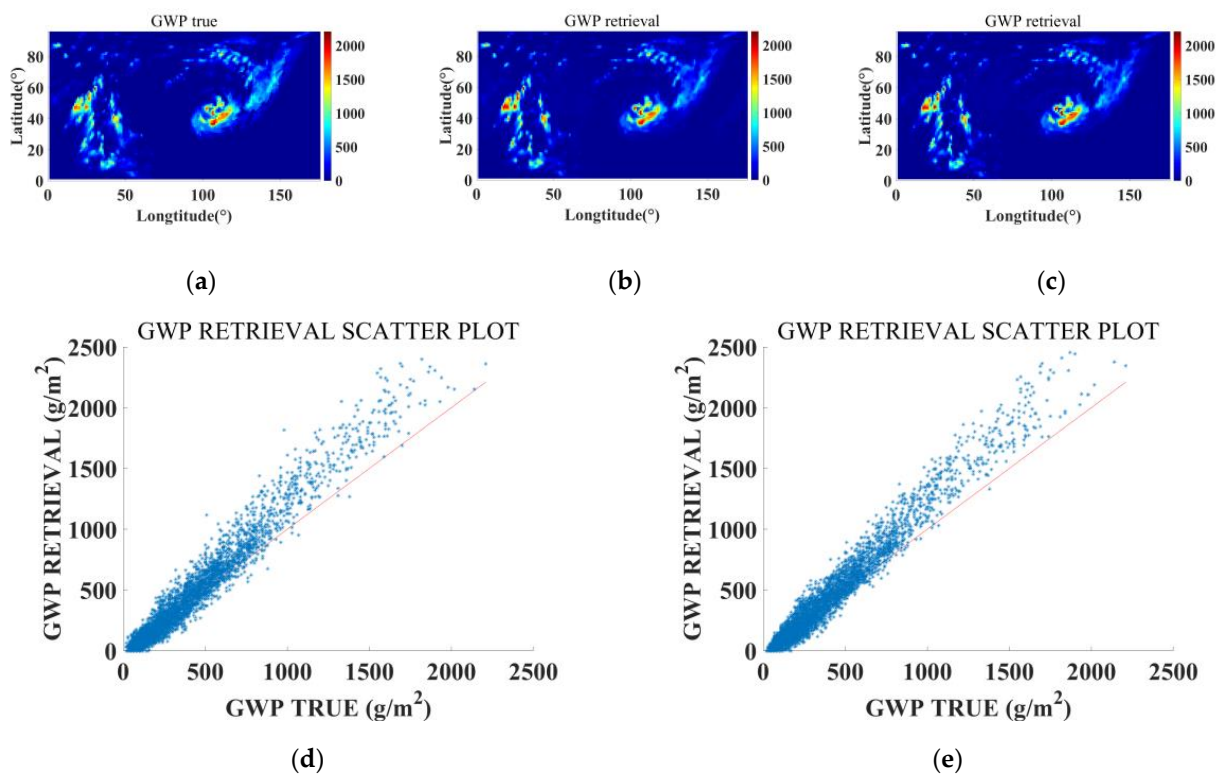


Figure 21. GWP retrieval results for the actual ATMS observation. (a) Reference truth; (b) Unet retrieval; (c) RCNN-ResUnet retrieval; (d) scatter plot of Unet retrieval; and (e) scatter plot of RCNN-ResUnet retrieval. The red line in (d,e) represents the function $y = x$.

Figure 22a,b show the percentage errors of GWP retrieved by Unet and RCNN–ResUnet, respectively, for all eight test scenarios, in which the blue bars represent the errors of the ATMS simulation and the red bars represent the ATMS observations. As shown in Figure 22a, when Unet is used in the ATMS simulation, the relative error in the GWP is between 17% and 32% for all test data, with an average of 24.92%. According to the Unet to ATMS observations, the relative error in the GWP is between 18% and 30% for all the test data, with an average of 26.27%, reflecting an increase of only 5.4% compared with the ideal value (ATMS simulation). As shown in Figure 22b, when RCNN–ResUnet is used in the ATMS simulation, the relative error in the GWP is between 14% and 43%, with an average of 28.56%. Using the RCNN–ResUnet for the ATMS observations, the relative error in the GWP is between 19% and 40% for all the test data, with an average of 30.74%, reflecting an increase of only 7.6% compared with the ideal value.

Figure 22 indicates that the proposed CNNs trained by the simulated brightness temperature can effectively retrieve the GWP from the actual ATMS millimeter scale brightness temperature. Compared with the ideal case, the retrieval error of GWP increases by 5.4% for Unet and 7.6% for RCNN–ResUnet. UNet outperforms RCNN–ResUnet slightly for all eight test scenarios, and the average error of RCNN–ResUnet is 17% greater than that of Unet.

4.2.2. Retrieval of Graupel Water Content (GWC)

Then, the CNN algorithms were applied to the simulated ATMS 183 GHz brightness temperature and the actual ATMS observation data to retrieve the GWC.

Figure 23 shows the GWC retrieval experimental results of the ATMS simulation for Typhoon SARIKA using Unet and RCNN–ResUnet, where (a) is the “reference truth” in the test data, (b) is the retrieval result of Unet, and (c) is the retrieval result of RCNN–ResUnet. Figure 24 shows the GWC retrieval experimental results for the actual ATMS observations, where (a) is the “reference truth” in the test data, (b) is the retrieval result of Unet, (c) is the retrieval result of RCNN–ResUnet, (d) is the scatter plot of Unet retrieval and (e) is the scatter plot of RCNN–ResUnet retrieval. Even for the actual ATMS observations, RCNN–ResUnet trained by the ATMS simulation can accurately retrieve the spatial distribution characteristics of the GWC, while the difference between the retrieval of the UNet and the reference truth is obviously greater.

Figure 25a,b show the percentage errors of the GWC retrieved by Unet and RCNN–ResUnet, respectively, for all eight test scenarios, in which the blue bars represent the errors of the ATMS simulation and the red bars represent the ATMS observations. As shown in Figure 25a, when Unet is used in the ATMS simulation, the relative error in the GWC is between 38% and 55% for all test data, with an average of 43.55%. According to the Unet to ATMS observations, the relative error in the GWP is between 41% and 70% for all the test data, with an average of 54.08%, an increase of 24% compared with the ideal (ATMS simulation). As shown in Figure 25b, when RCNN–ResUnet is used in the ATMS simulation, the relative error in the GWC is between 28% and 46%, with an average of 34.78%. Using the RCNN–ResUnet for the ATMS observations, the relative error in the GWP is between 32% and 55% for all the test data, with an average of 40.88%, an increase of 17.5% compared with the ideal value.

Figure 25 indicates that the proposed CNNs trained by the simulated brightness temperature can effectively retrieve the GWP from the actual ATMS millimeter scale brightness temperature. Compared with the ideal case, the retrieval error of GWP increases by 24% for Unet and 17.5% for RCNN–ResUnet. RCNN–ResUnet outperforms Unet for all eight test scenarios, and the average error of Unet is 32% greater than that of RCNN–ResUnet.

4.2.3. The Sensitivity Experiments for the Retrieval of Graupel Parameters

To demonstrate the sensitivity of the established CNN model to brightness temperature observation errors, sensitivity experiments for the retrieval of graupel parameters from

ATMS observations have been conducted. In the sensitivity experiments, the simulated ATMS brightness temperature for retrieval test was added with 0.5 times, 1 times, and 2 times the standard NEDT noise, respectively (the specific NEDT values of each frequency channel are shown in Table 3). Table 7 shows the sensitivity experimental results for GWP retrieval. As can be seen, compared with the result without noise, the Unet retrieval errors with 0.5 times noise, 1 times noise, and 2 times noise increase by 1.48%, 3.93%, and 13.72%, respectively, and the RCNN–ResUnet retrieval errors increase by 1.79%, 5.46%, and 17.58%, respectively. Table 8 shows the sensitivity experimental results for GWC retrieval. Compared with the result without noise, the Unet retrieval errors with 0.5 times noise, 1 times noise, and 2 times noise increase by 1.81%, 6.61%, and 20.09%, respectively, and the RCNN–ResUnet retrieval errors increase by 3.02%, 11.33%, and 36.72%, respectively.

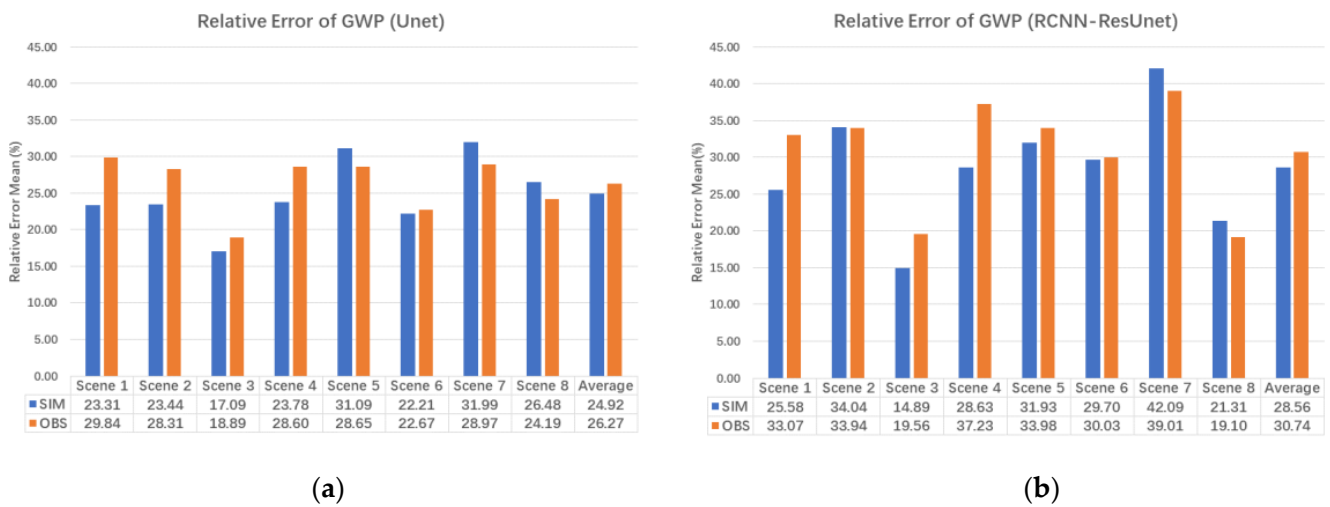


Figure 22. Relative errors in GWP for all eight tropical cyclone scenarios. (a) Unet and (b) RCNN–ResUnet. SIM stands for Simulation Temperature, OBS stands for Observation Temperature.

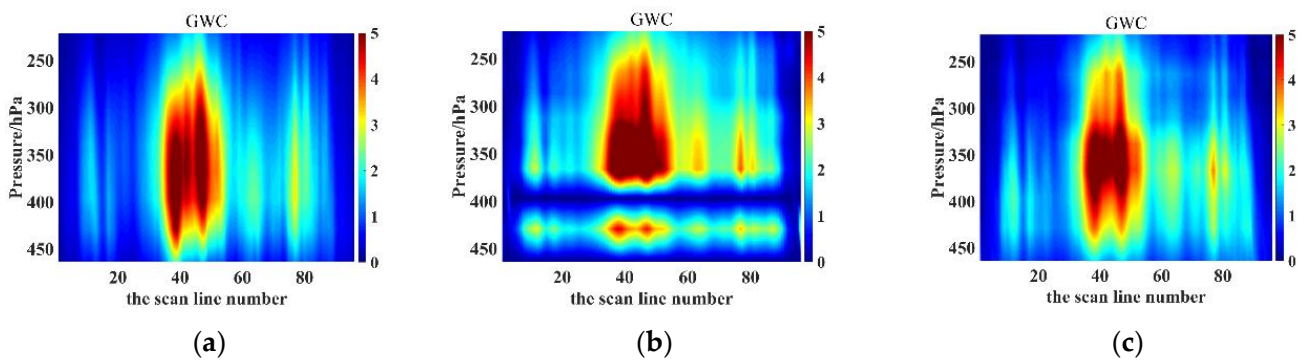


Figure 23. GWC retrieval results of the ATMS simulation. (a) Reference truth; (b) Unet retrieval; and (c) RCNN–ResUnet retrieval. The red line in (d,e) represents the function $y = x$.

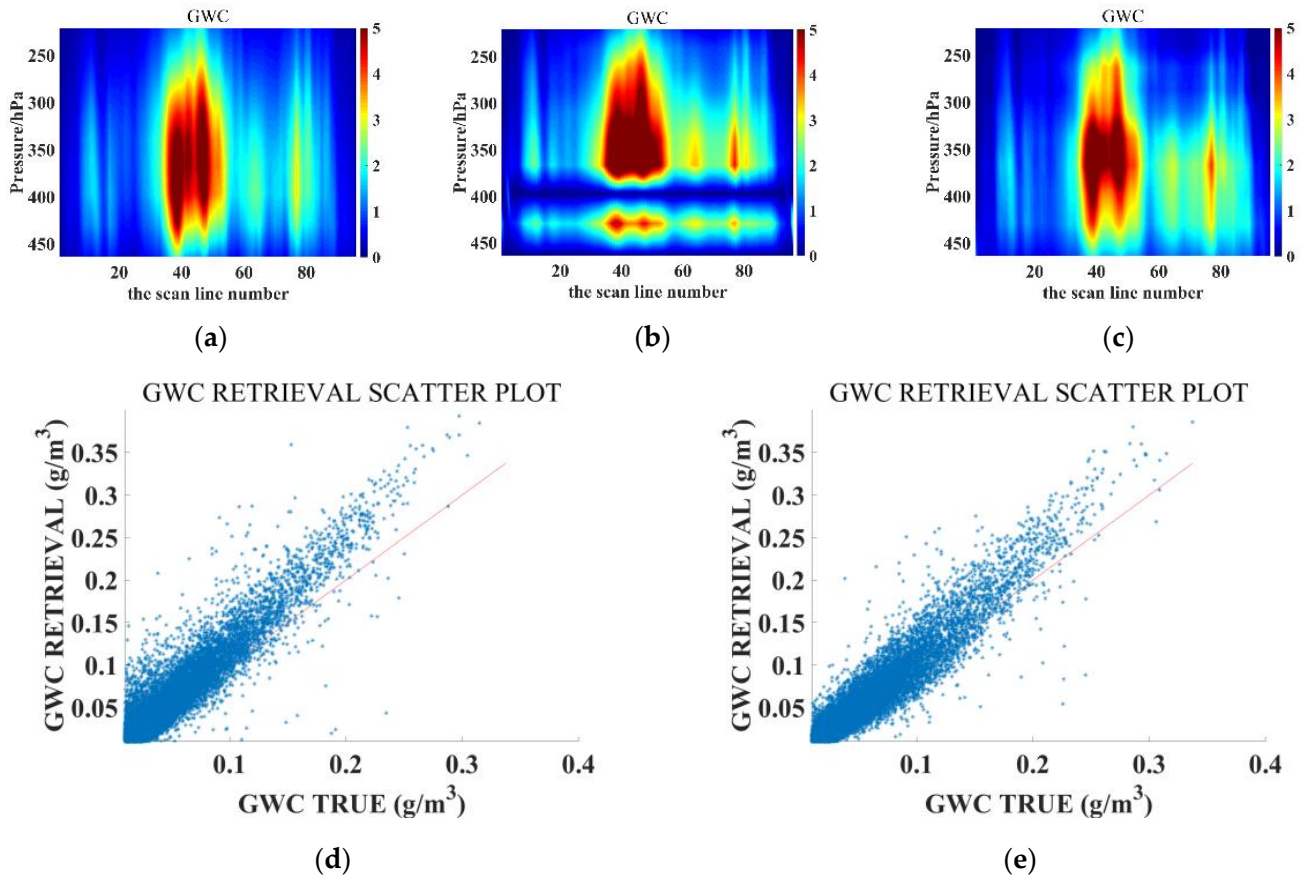


Figure 24. GWC retrieval results for the ATMS observation. (a) Reference truth; (b) Unet retrieval; (c) RCNN-ResUnet retrieval; (d) scatter plot of Unet retrieval; and (e) scatter plot of RCNN-ResUnet retrieval. The red line in (d,e) represents the function $y = x$.

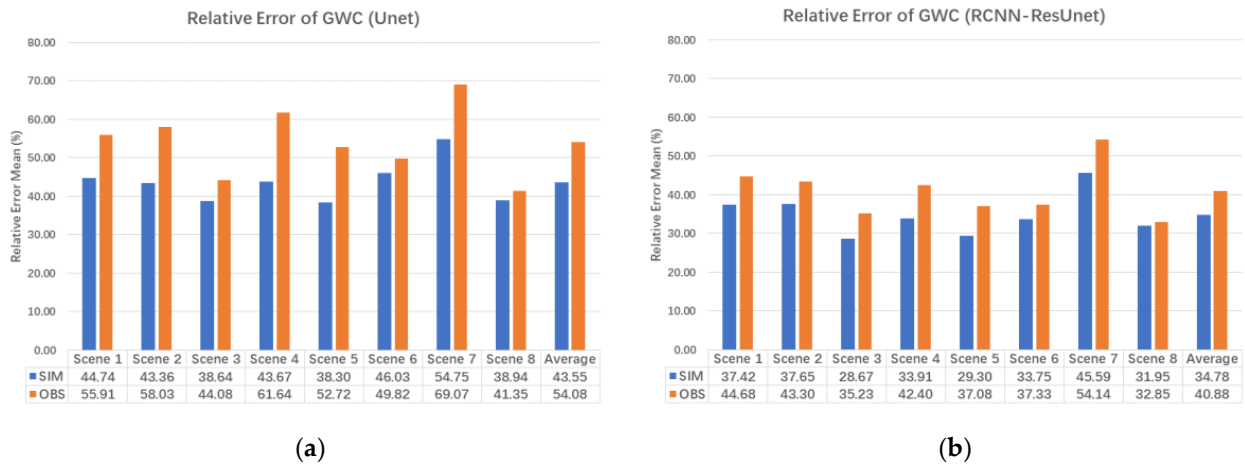


Figure 25. Relative errors in GWC for all eight tropical cyclone scenarios. (a) Unet and (b) RCNN-ResUnet. SIM stands for Simulation Temperature, OBS stands for Observation Temperature.

Table 7. Sensitivity experimental results for GWP retrieval.

| Average Relative Error (%) | No Noise | Add Noise (Half NEDT) | Add Noise (NEDT) | Add Noise (Double NEDT) |
|----------------------------|----------|-----------------------|------------------|-------------------------|
| Unet | 24.92 | 25.29 | 25.90 | 28.34 |
| RCNN-ResUnet | 28.56 | 29.07 | 30.12 | 33.58 |

Table 8. Sensitivity experimental results for GWC retrieval.

| Average Relative Error (%) | No Noise | Add Noise (Half NEDT) | Add Noise (NEDT) | Add Noise (Double NEDT) |
|----------------------------|----------|-----------------------|------------------|-------------------------|
| Unet | 43.55 | 44.34 | 46.43 | 52.30 |
| RCNN–ResUnet | 34.78 | 35.83 | 38.72 | 47.55 |

The sensitivity experimental results show that the performance of the CNN model will be significantly degraded if the observation noise is too large, but for the actual observation noise of ATMS, the retrieval error increase is small, indicating that the robustness of the CNN model can meet the needs of practical applications.

4.3. Comparison of the Retrieval Performance of Unet and RCNN–ResUnet

A comparison of the retrieval results of Unet and RCNN–ResUnet shows that RCNN–ResUnet outperforms Unet in all multiple species of ice hydrometeor retrieval experiments. In addition, for the vertical distribution of the ice hydrometeors, regardless of whether the ICI simulation or actual ATMS observation was used, the retrieved images (Figure 16, Figure 17, Figure 18, Figure 24, and Figure 25) of RCNN–ResUnet were obviously more consistent with the reference truth than those of Unet. Only for the GWP are the retrieval errors of Unet slightly smaller than those of RCNN–ResUnet.

The above experimental results indicate that the improved RCNN–ResUnet can learn more complex data features and perform better for more complex retrieval problems, such as multiple species of ice hydrometeor retrieval and profile retrieval, while Unet only shows good performance for simpler retrieval problems, such as the graupel water path (GWP).

There are several reasons why RCNN–ResUnet has better performance for complex retrieval problems: 1. RCNN–ResUnet adds an extra recurrent unit on top of Unet to capture contextual information in the images; 2. RCNN–ResUnet uses residual connections and multiscale features, which can help the network learn and represent cloud features at different scales better, while Unet has only regular skip connections; 3. The RCNN–ResUnet network architecture is deeper and has stronger feature learning and representation capabilities, while Unet is relatively shallow. By introducing recurrent units, residual connections and other methods, RCNN–ResUnet has significantly improved model expression and feature extraction abilities compared to Unet. Therefore, this approach achieves better performance for the multiple species of ice hydrometeor retrieval task.

5. Conclusions and Discussion

For the first time, we present the use of deep convolutional neural networks for the joint retrieval of multiple species of ice hydrometeors (ice, snow, and graupel) (XWP and XWC) from millimeter and submillimeter wave brightness temperatures, particularly for future ICI data. The improved RCNN–ResUnet uses a recurrent unit to enhance feature representation and to better learn and represent cloud features at different scales with residual connections and multiscale features. Networks were trained on the simulated ICI brightness temperature dataset covering all tropical cyclones passing through China’s coastal regions from 2016 to 2022, and samples including tropical cyclones across all intensity levels were tested with great accuracy. Good experimental results were obtained compared with those of the classical Unet. The average relative errors are 14.48% for GWP, 51.38% for IWP, 57.01% for SWP, 18.41% for GWC, 68.84% for IWC, and 78.06% for SWC. Compared with the previous study of Eriksson et al. [23], the average relative error of the total content retrieved by RCNN–ResUnet is reduced by 71%. Compared with the previous study of Chen et al. [24], the average relative error of the vertical profiles retrieved by RCNN–ResUnet is reduced by 69%.

The CNNs trained by the simulated brightness temperature were also applied to the actual ATMS observed millimeter wave brightness temperature to retrieve the GWP and GWC, with average relative errors of 30.74% for the GWP and 40.88% for the GWC,

increasing by 7.6% and 17.5%, respectively, compared with the ideal values. The ATMS observation retrieval experiment results show that the forward model that generates a simulated brightness temperature dataset can calculate the actual radiative transfer process with good accuracy, so the network learning from the simulation dataset can obtain a good retrieval capability for real observations. This also shows the feasibility of applying RCNN–ResUnet trained by ICI simulation to future ICI observation. We conclude that a deep network is an appropriate learning paradigm for the statistical retrieval of multiple species of ice hydrometeor parameters.

In addition, the retrieval results for multiple species of ice hydrometeors revealed that the relative errors in ice and snow are much larger than those in graupel for both networks. Compared to that of ice and snow particles, the relative error in the GWP is only approximately one-quarter. From the reference truth value, the total amount and particle size of ice and snow particles are much smaller than those of graupel, resulting in the brightness temperature changes of 11 frequency channels of ICI caused by ice and snow also being smaller than those of graupel. Therefore, in the training process of the CNN network, the features of ice and snow in the data set are much weaker than those of graupel and are even submerged by the strong features of graupel, which may be the reason why the retrieval error of ice and snow is much larger than that of graupel. This will be the direction of future improvement of joint retrieval algorithm based on CNN.

Future work will also improve retrieval accuracy and expand parameter types to provide support for future submillimeter wave radiometers used for ice cloud remote sensing.

Author Contributions: Formal analysis, Y.C.; investigation, K.C. and J.W.; methodology, K.C.; software, J.W.; validation, Y.C.; writing—original draft, K.C. and J.W.; writing—review and editing, K.C. All authors have read and agreed to the published version of the manuscript.

Funding: This research was supported by the National Natural Science Foundation of China (Grant Nos. 42275141 and 42276183).

Data Availability Statement: Data are contained within the article.

Acknowledgments: The authors thank Al. Gasiewski from the University of Colorado at Boulder for sharing the DOTLRT model. The authors also thank the ECMWF for providing the ERA5 reanalysis data. The authors also thank the NCAR for sharing the WRF codes.

Conflicts of Interest: The authors declare no conflicts of interest.

References

1. Wang, H.; Duan, C.; Lv, R.; Lei, H.; Zhu, Z.; Chen, G. Development and Problems of Spaceborne Terahertz Ice Cloud Detection Technology. *J. Terahertz Sci. Electron. Inf. Technol.* **2017**, *5*, 722–727.
2. Zhang, X.; Hu, W.; Liu, R.; Si, W.; Li, Y.; Liu, Y.; Ligthart, L.P. Design of 874 GHz Ice Cloud Detection Instrument Based on Cubesat Platform. *Aerosp. Shanghai* **2018**, *35*, 144–150.
3. Buehler, S.A.; Jiménez, C.; Evans, K.F.; Eriksson, P.; Rydberg, B.; Heymsfield, A.J.; Stubenrauch, C.J.; Lohmann, U.; Emde, C.; John, V.O.; et al. A concept for a satellite mission to measure cloud ice water path, ice particle size, and cloud altitude. *Q. J. R. Meteorol. Soc. J. Atmos. Sci. Appl. Meteorol. Phys. Oceanogr.* **2007**, *133*, 109–128. [[CrossRef](#)]
4. Liou, K.-N. Influence of cirrus clouds on weather and climate processes: A global perspective. *Mon. Weather. Rev.* **1986**, *114*, 1167–1199. [[CrossRef](#)]
5. Njoku, E. Passive microwave remote sensing of the earth from space—A review. *Proc. IEEE* **1982**, *70*, 728–750. [[CrossRef](#)]
6. Gustavsson, K.; Sheikh, M.Z.; Naso, A.; Pumar, A.; Mehlig, B. Effect of particle inertia on the alignment of small ice crystals in turbulent clouds. *J. Atmos. Sci.* **2021**, *78*, 2573–2587. [[CrossRef](#)]
7. Skolnik, M.I. Millimeter and submillimeter wave applications. In Proceedings of the Symposium on Submillimeter Waves, Polytechnic Press of Poly, New York, NY, USA, 31 March–2 April 1970; Institute of Brooklyn: New York, NY, USA, 1970.
8. Kidder, S.Q.; Goldberg, M.D.; Zehr, R.M.; DeMaria, M.; Purdom, J.F.W.; Velden, C.S.; Grody, N.C.; Kusselson, S.J. Satellite analysis of tropical cyclones using the Advanced Microwave Sounding Unit (AMSU). *Bull. Am. Meteorol. Soc.* **2000**, *81*, 1241–1259. [[CrossRef](#)]
9. Bonsignori, R. The Microwave Humidity Sounder (MHS): In-orbit performance assessment. In Proceedings of the Sensors, Systems, and Next-Generation Satellites XI, Florence, Italy, 17–20 September 2007; p. 67440A.

10. Weng, F.; Zou, X.; Wang, X.; Yang, S.; Goldberg, M.D. Introduction to Suomi national polar-orbiting partnership advanced technology microwave sounder for numerical weather prediction and tropical cyclone applications. *J. Geophys. Res. Atmos.* **2012**, *117*, D19112. [[CrossRef](#)]
11. Chen, K.; English, S.; Bormann, N.; Zhu, J. Assessment of FY-3A and FY-3B MWS observations. *Weather Forecast.* **2015**, *30*, 1280–1290. [[CrossRef](#)]
12. Zou, X.; Wang, X.; Weng, F.; Li, G. Assessments of Chinese Fengyun Microwave Temperature Sounder (MWTS) measurements for weather and climate applications. *J. Atmos. Ocean. Technol.* **2011**, *28*, 1206–1227. [[CrossRef](#)]
13. Kangas, V.; D’Addio, S.; Klein, U.; Loiselet, M.; Mason, G.; Orlhac, J.C.; Gonzalez, R.; Bergada, M.; Brandt, M.; Thomas, B. Ice cloud imager instrument for MetOp Second Generation. In Proceedings of the 2014 13th Specialist Meeting on Microwave Radiometry and Remote Sensing of the Environment (MicroRad), Pasadena, CA, USA, 24–27 March 2014.
14. Schlüssel, P.; Kayal, G. Introduction to the next generation EUMETSAT polar system (EPS-SG) observation missions. In Proceedings of the Conference on Sensors, Systems, and Next-Generation Satellites XX, Warsaw, Poland, 11–14 September 2017.
15. Evans, K.F.; Graeme, L.S. Microwave radiative transfer through clouds composed of realistically shaped ice crystals. Part I. Single scattering properties. *J. Atmos. Sci.* **1995**, *52*, 2041–2057.
16. Evans, K.F.; Stephens, G.L. Microwave radiative transfer through clouds composed of realistically shaped ice crystals. Part II. Remote sensing of ice clouds. *J. Atmos. Sci.* **1995**, *52*, 2058–2072. [[CrossRef](#)]
17. Evans, K.F.; Wang, J.R.; O’C Starr, D.; Heymsfield, G.; Li, L.; Tian, L.; Lawson, R.P.; Heymsfield, A.J.; Bansemmer, A. Ice hydrometeor profile retrieval algorithm for high-frequency microwave radiometers: Application to the CoSSIR instrument during TC4. *Atmos. Meas. Tech.* **2012**, *5*, 2277–2306. [[CrossRef](#)]
18. Buehler, S.A.; Eriksson, P.; Kuhn, T.; von Engeln, A.; Verdes, C. ARTS, the atmospheric radiative transfer simulator. *J. Quant. Spectrosc. Radiat. Transf.* **2005**, *91*, 65–93. [[CrossRef](#)]
19. Jiménez, C.; Buehler, S.A.; Rydberg, B.; Eriksson, P.; Evans, K.F. Performance simulations for a submillimetre-wave satellite instrument to measure cloud ice. *Q. J. R. Meteorol. Soc. J. Atmos. Sci. Appl. Meteorol. Phys. Oceanogr.* **2007**, *133*, 129–149. [[CrossRef](#)]
20. Weng, F.; Grody, N.C. Retrieval of ice cloud parameters USING a microwave imaging radiometer. *J. Atmos. Sci.* **2000**, *57*, 1069–1081. [[CrossRef](#)]
21. Dong, P.; Liu, L.; Li, S.; Husi, L.; Hu, S.; Bu, L. A novel Ice Cloud Retrieval Algorithm for Sub-Millimeter Wave Radiometers: Simulations and Application to an Airborne Experiment. *IEEE Trans. Geosci. Remote Sens.* **2023**, *61*, 2001609. [[CrossRef](#)]
22. Li, M.; Letu, H.; Ishimoto, H.; Li, S.; Liu, L.; Nakajima, T.Y.; Ji, D.; Shang, H.; Shi, C. Retrieval of terahertz ice cloud properties from airborne measurements based on the irregularly shaped Voronoi ice scattering models. *Atmos. Meas. Tech.* **2023**, *16*, 331–353. [[CrossRef](#)]
23. Eriksson, P.; Rydberg, B.; Mattioli, V.; Thoss, A.; Accadia, C.; Klein, U.; Buehler, S.A. Towards an operational Ice Cloud Imager (ICI) retrieval product. *Atmos. Meas. Tech.* **2020**, *13*, 53–71. [[CrossRef](#)]
24. Chen, K.; Zhang, L.; Zhang, Y.; Dong, S.; Liu, Y.; Wu, Q.; Shang, J. Study on Terahertz Ice Cloud Detection Inversion Algorithm Based on Neural Network. *J. Remote Sens.* **2022**, *26*, 2043–2059.
25. Powers, J.G.; Klemp, J.B.; Skamarock, W.C.; Davis, C.A.; Dudhia, J.; Gill, D.O.; Coen, J.L.; Gochis, D.J.; Ahmadov, R.; Peckham, S.E.; et al. The weather research and forecasting model: Overview, system efforts, and future directions. *Bull. Am. Meteorol. Soc.* **2017**, *98*, 1717–1737. [[CrossRef](#)]
26. Bauer, P.; Moreau, E.; Chevallier, F.; O’keeffe, U. Multiple-scattering microwave radiative transfer for data assimilation applications. *Q. J. R. Meteorol. Soc. J. Atmos. Sci. Appl. Meteorol. Phys. Oceanogr.* **2006**, *132*, 1259–1281. [[CrossRef](#)]
27. Voronovich, A.; Gasiewski, A.; Weber, B. A fast multistream scattering-based Jacobian for microwave radiance assimilation. *IEEE Trans. Geosci. Remote Sens.* **2004**, *42*, 1749–1761. [[CrossRef](#)]
28. O’Shea, K.; Nash, R. An introduction to convolutional neural networks. *arXiv* **2015**, arXiv:1511.08458.
29. Guo, Y.; Chen, E.; Guo, Y.; Li, Z.; Li, C.; Xu, K. Deep highway unit network for land cover type classification with GF-3 SAR imagery. In Proceedings of the 2017 SAR in Big Data Era: Models, Methods and Applications (BIGSAR DATA), Beijing, China, 13–14 November 2017; pp. 1–6.
30. Pai, M.M.; Mehrotra, V.; Aiyar, S.; Verma, U.; Pai, R.M. Automatic segmentation of river and land in sar images: A deep learning approach. In Proceedings of the 2019 IEEE Second International Conference on Artificial Intelligence and Knowledge Engineering (AIKE), Sardinia, Italy, 3–5 June 2019.
31. Yao, Q.; Hu, X.; Lei, H. Multiscale convolutional neural networks for geospatial object detection in VHR satellite images. *IEEE Geosci. Remote Sens. Lett.* **2020**, *18*, 23–27. [[CrossRef](#)]
32. Wang, L.; Scott, K.A.; Clausi, D.A. Sea ice concentration estimation during freeze-up from SAR imagery using a convolutional neural network. *Remote Sens.* **2017**, *9*, 408. [[CrossRef](#)]
33. Cooke, C.L.V.; Scott, K.A. Estimating sea ice concentration From SAR: Training convolutional neural networks with passive microwave data. *IEEE Trans. Geosci. Remote Sens.* **2019**, *57*, 4735–4747. [[CrossRef](#)]
34. Tan, J.; NourEldeen, N.; Mao, K.; Shi, J.; Li, Z.; Xu, T.; Yuan, Z. Deep learning convolutional neural network for the retrieval of land surface temperature from AMSR2 DATA in China. *Sensors* **2019**, *19*, 2987. [[CrossRef](#)] [[PubMed](#)]
35. Tan, J.C. Research on Inversion Methods of Key Parameters for Water Conservation Based on Remote Sensing Data. Master’s Thesis, Chinese Academy of Agricultural Sciences, Beijing, China, 2019.

36. Hersbach, H.; Bell, B.; Berrisford, P.; Hirahara, S.; Horányi, A.; Muñoz-Sabater, J.; Nicolas, J.; Peubey, C.; Radu, R.; Schepers, D.; et al. The ERA5 global reanalysis. *Q. J. R. Meteorol. Soc.* **2020**, *146*, 1999–2049. [[CrossRef](#)]
37. Zhou, L.; Divakarla, M.; Liu, X. An overview of the Joint Polar Satellite System (JPSS) science data product calibration and validation. *Remote Sens.* **2016**, *8*, 139. [[CrossRef](#)]
38. Chen, K.; Dong, S.; Li, Y.; Xu, H.; Xie, Z.; Jiang, L.; Li, E.; Wu, Q.; Shang, J. Study on Terahertz Ice Cloud Radiation Scattering Characteristics and Detection Parameter Design. *J. Remote Sens.* **2022**, *26*, 2204–2218.
39. Lang, S.E.; Tao, W.K.; Zeng, X.; Li, Y. Reducing the biases in simulated radar reflectivities from a bulk microphysics scheme: Tropical convective systems. *J. Atmos. Sci.* **2011**, *68*, 2306–2320. [[CrossRef](#)]
40. Heymsfield, A.J.; Jaquinta, J. Cirrus crystal terminal velocities. *J. Atmos. Sci.* **2000**, *57*, 916–938. [[CrossRef](#)]
41. Ronneberger, O.; Fischer, P.; Brox, T. U-net: Convolutional networks for biomedical image segmentation. In Proceedings of the Medical Image Computing and Computer-Assisted Intervention—MICCAI 2015: 18th International Conference, Munich, Germany, 5–9 October 2015; Proceedings, Part III 18. Springer International Publishing: Munich, Germany, 2015.
42. Wan, C.; Wu, J.; Li, H.; Yan, Z.; Wang, C.; Jiang, Q.; Cao, G.; Xu, Y.; Yang, W. Optimized-Unet: Novel algorithm for parapapillary atrophy segmentation. *Front. Neurosci.* **2021**, *15*, 758887. [[CrossRef](#)] [[PubMed](#)]
43. Diakogiannis, F.I.; Waldner, F.; Caccetta, P.; Wu, C. ResUNet-a: A deep learning framework for semantic segmentation of remotely sensed data. *ISPRS J. Photogramm. Remote Sens.* **2020**, *162*, 94–114. [[CrossRef](#)]
44. Zhou, Z.; Siddiquee, M.M.R.; Tajbakhsh, N.; Liang, J. UNet++: Redesigning skip connections to exploit multiscale features in image segmentation. *IEEE Trans. Med. Imaging* **2020**, *39*, 1856–1867. [[CrossRef](#)]
45. Lian, S.; Luo, Z.; Zhong, Z.; Lin, X.; Su, S.; Li, S. Attention guided U-Net for accurate iris segmentation. *J. Vis. Commun. Image Represent.* **2018**, *56*, 296–304. [[CrossRef](#)]
46. Liang, M.; Hu, X. Recurrent convolutional neural network for object recognition. In Proceedings of the IEEE Conference on Computer Vision and Pattern Recognition, Boston, MA, USA, 7–12 June 2015.
47. He, K.; Zhang, X.; Ren, S.; Sun, J. Deep residual learning for image recognition. In Proceedings of the IEEE Conference on Computer Vision and Pattern Recognition, Las Vegas, NV, USA, 27 June–1 July 2016.

Disclaimer/Publisher’s Note: The statements, opinions and data contained in all publications are solely those of the individual author(s) and contributor(s) and not of MDPI and/or the editor(s). MDPI and/or the editor(s) disclaim responsibility for any injury to people or property resulting from any ideas, methods, instructions or products referred to in the content.